Absolute N-atom density measurement in an Ar/N2 micro-hollow cathode discharge jet by means of ns-two-photon absorption laser-induced fluorescence

A Remigy, X Aubert, Swaminathan Prasanna, K Gazeli, L Invernizzi, G Lombardi, C Lazzaroni

Absolute N atom density measurement in a Ar/N_2 Micro Hollow Cathode Discharge jet by means of ns-Two-photon Absorption Laser Induced Fluorescence

A. Remigy,[1] X. Aubert,[1] S. Prasanna,[1] K. Gazeli,[1] L. Invernizzi,[1] G. Lombardi,[1] and C. Lazzaroni[1]
Université Sorbonne Paris Nord, Laboratoire des Sciences des Procédés et des Matériaux, LSPM, CNRS, UPR 3407, F-93430, Villetaneuse, France

(*Electronic mail: claudia.lazzaroni@lspm.cnrs.fr)

(Dated: 23 September 2022)

In this work, nanosecond Two-photon Absorption Laser Induced Fluorescence (TALIF) is used to probe the absolute density of nitrogen atoms in a plasma generated using a micro-hollow cathode discharge (MHCD). The MHCD is operated in the normal regime and the plasma is ignited in an Ar/N_2 gas mixture. First, we study a MHCD configuration having the same pressure (50 mbar) on both sides of the electrodes. A good agreement is found between the density of N atoms measured using TALIF in this work, and previous measurements using vacuum ultraviolet Fourier transform absorption spectroscopy. Then, we introduce a pressure differential between the two electrodes of the MHCD, creating a plasma jet. The influence of the discharge current, the percentage of N_2 in the gas mixture and pressures on both sides of the MHCD is studied. The current has a small impact on the N-atoms density. Furthermore, an optimal N-atom density is found at around 95% of N_2 in the discharge. Finally, we demonstrate that the pressure has a different impact depending on the side of the MHCD: the density of N-atoms is much more sensitive to the change of the pressure in the low pressure side when compared to the pressure change in the high pressure side. This could be due to several competing phenomena: gas residence time in the cathodic region, recirculation or recombination of the N-atoms at the wall. This study contributes to the optimization of MHCD as an efficient N-atom source for material deposition applications.

I. INTRODUCTION

Nitrogen is a crucial atom in many material deposition applications, from III-V nitride semiconductors such as GaN, AlGaN or InGaN[1–3], used in microelectronics and photonics[4,5], to nitrogen-doped diamond and NV centers for quantum application[6], and hexagonal boron nitride (h-BN) as a substrate for graphene based technologies[7,8]. Synthesis of such materials requires sources of nitrogen (N) atoms that can produce high densities over large surfaces, most of the time at low pressure to promote surface mobility at the substrate where the growth occurs. To do so, many different plasma configurations have been used, for instance, microwave plasma[9], inductively coupled plasma[10], ECR plasma[11] or radio-frequency plasma[12]. Although that these sources allow for large plasma volumes to be produced, they operate at a rather high power of at least few hundreds watts. On the opposite, microplasmas, which are usually defined as plasmas with at least one dimension lower than 1 mm, have attracted a lot of attention[13,14] as they can be generated at much lower powers (1 W), provide high electron density and, thus, rich chemical reactivity, while maintaining the plasma volume at the microscale level. Micro-Hollow Cathode Discharges (MHCD) represent a particular geometries of microplasmas, in which a hole of a few hundreds micrometers in diameter is drilled through an electrode-dielectric-electrode structure[15]. When supplied with a simple DC power, a plasma ignites in the hole and can be sustained in different regimes depending on the discharge current[16]. At low current (typically 0.1 to 0.5 mA), even if the discharge is DC power driven, an unstable and oscillating regime appears (self-pulsing regime), which leads to pulsed discharge voltage and current signals. At higher current ($>$ 1 mA), however, the plasma becomes stable, with continuous voltage and current, and it expands on the cathodic surface (normal regime). This plasma source has been shown to produce high electron densities[17,18] (up to 10^{22} m^{-3}) and high density of N atoms (up to few 10^{19} m^{-3} in the normal regime[19]). Typically, the plasma volume generated by MHCD is confined in a micrometric hole. To implement it in applications requiring large plasma volumes, it is possible to achieve the generation of a large afterglow discharge, which makes the MHCD a versatile plasma source. The plasma volume of MHCDs can be extended using different techniques: creating a plasma jet[20], using an array of MHCDs[21], and even using a third electrode to expand the plasma outside the hole, which is known as the Micro-Cathode Sustained Discharge (MCSD)[22,23]. The latter solution has been successfully used to produced h-BN films over 2-inches diameter substrates[24]. When targeting nitride deposition, precise measurements of the N atoms density in these discharges are needed. However, the characterization of such plasmas is challenging due to their small dimensions, which demands non intrusive techniques with high spatial resolution. The ground state of atomic nitrogen $(2p^3)$ $^4S^0_{3/2}$ is only accessible in the vacuum ultraviolet (VUV) range, which can be probed using absorption spectroscopy, but it requires a UV radiation source and vacuum environment. To circumvent the need for VUV facilities, Two-photon Absorption Laser Induced Fluorescence (TALIF) was introduced and successfully used to probe the density of N atoms in various plasma sources[25,26]. TALIF is a highly sensitive technique with a very good spatial and temporal resolution.

In this paper, we report on TALIF measurements of the N atoms density in a MHCD-generated plasma operated in the

normal regime in a gas mixture of argon (Ar) and molecular nitrogen (N_2). Addition of small quantities of argon to the discharge may enhance the dissociation of N_2 and increases the lifespan of the MHCD device. The MHCD is first studied without a pressure differential, to compare with a previous study of the N atoms density performed using absorption spectroscopy[19]. We then introduce a pressure differential to increase the plasma volume, which is useful when targeting an application of the MHCD source in material deposition. Here, we study the impact of the introduction of this pressure differential on the production of N atoms. The impact of the gas mixture, the discharge current and variation of the pressure differential on the production and propagation of N atoms is also studied. Section II describes the plasma reactor and the TALIF experimental setup used to characterize it. Section III explains the methodology used to perform quantitative measurements of the N atoms absolute density in the plasma. The parametric study and discussion are presented in section IV while section V closes the paper with the conclusion.

II. EXPERIMENTAL SETUP

A. Plasma source

A scheme of the MHCD studied in this work is illustrated in Figure 1. It consists of an assembly of a 750 μm thick alumina (Al_2O_3) dielectric plate, in between two 100 μm thick molybdenum (Mo) electrodes. This assembly is glued with a heat-resistant epoxy glue, and then laser pierced with a 400 μm diameter hole. The source is placed at the junction of the two chambers of a reactor, as represented in Fig.1. A pipe with a valve, links the two chambers, allowing them to operate either at the same pressure (when the valve is open), or with a pressure differential (when the valve is closed). Using two gas flowmeters, an Ar/N_2 gas mixture is injected in the upstream chamber, and a primary pump with a manual valve is installed in the downstream chamber. The pressure of both chambers can be regulated by adjusting the gas fluxes delivered by the flowmeters and the pumping using the manual valve.

To ignite the plasma, a negative DC power supply (0 - 2000 V) is used. A negative high voltage is applied to the cathode in the upstream chamber, while the anode (downstream chamber) is grounded. When a pressure differential is set between the two chambers, a plasma jet appears on the anodic side, as depicted in Fig. 1 and visible in the photograph of Fig.1.

A ballast resistor R_b = 480 kΩ is connected between the power source and the cathode to limit the discharge current I_d. The discharge voltage V_d is monitored using a voltage probe placed after R_b. Between the anode and the ground, a small resistor R_m = 180 Ω is used to measure the discharge current. Another voltage probe measures V_1, i.e. the voltage across R_m, which can then be used to calculate the corresponding discharge current. The pair (V_d, I_d) is defined by the plasma conditions and, thus, V_d and I_d cannot be set independently. In this study, we use the current I_d as a reference and the corresponding discharge voltage V_d is defined by the plasma conditions. In the range of electrical conditions covered here, the MHCD is operating in the normal regime with continuous discharge current and voltage signals.

B. TALIF diagnostic setup

The density of N atoms produced by the plasma source investigated in this study is evaluated using a ns-TALIF setup, described hereafter, and applied in a large range of plasma conditions. The $\vec{x}$ and $\vec{y}$ axis vectors used to determine the position at which the measurements are done are represented in Fig.1. To perform spatial measurements, the reactor is placed on a test bench as represented in Figure 2 (see next sections for a more detailed description). The reactor is equipped with two fused silica windows, providing a 90% transmission at 205 nm, so that the laser radiation can reach the plasma. The fluorescence is collected perpendicularly to the laser line-of-sight through a borosilicate window.

1. Laser system

The ns-TALIF setup is represented in Fig. 2. The laser used is a tunable dye laser (SirahLasertechnik Cobra-Stretch) pumped by the second harmonic of a 500 mJ/pulse Nd:YAG laser (Spectra Physics Quanta-Ray Lab-Series 170-01). The Nd:YAG laser pulses at 10 Hz and provides a pulse with a width of 7 ns measured by means of the photodiode PD1. Two β-barium borate (BBO) crystals process the dye laser beam in the Frequency Conversion Unit (FCU) to yield a three-harmonic laser beam. These harmonics are separated using two fused silica Pellin-Broca prisms, to spatially select the third harmonic, which is used in our experiments. Its wavelength can be tuned between 204 and 207 nm, and has a typical energy of 2.5 mJ/pulse. The visible harmonic of the beam coming out of the FCU is directed towards a iodine cell (I_2 cell). The laser wavelength is systematically calibrated using the known absorption profile of the cell as a function of the laser wavelength. The UV-C beam obtained is directed towards the reactor using a periscope and focused at the center of the reactor using a 35 cm-focal-length lens. When exiting the reactor, the laser beam is collimated onto a calorimeter (Coherent J-10MB-LE), which is connected to an oscilloscope (Lecroy WaveJet 354-A, 500 MHz, 2 GS/s) in order to record the laser energy. It was verified that the absorption of the laser by the plasma is negligible beforehand, with no difference on the energy measured with and without plasma. That is due to the small cross-section of the two-photon absorption process. More so than the plasma, the optical windows of the reactor do absorb a part of the laser radiation. The energy of the laser beam in the reactor is calculated from the energy measured outside the reactor by considering the transmittance of the optical windows. The laser focal spot size can be calculated from its wavelength and the characteristics of the optics[27]. With a beam diameter before the lens of 5 mm, the minimum waist of the laser is calculated to be of 5 μm. The Rayleigh length is 300 μm. The volume of interaction between the laser and

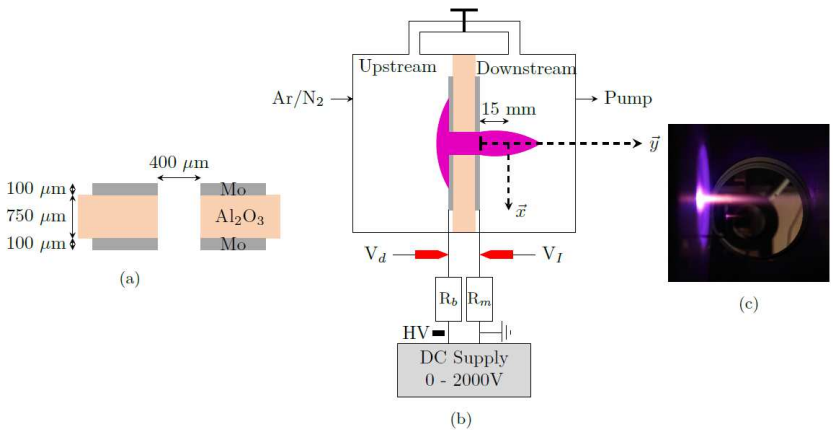

FIG. 1. Scheme of (a) the MHCD configuration and (b) the reactor used in the experiments. R_b = 480 kΩ, R_m = 180 Ω, HV = High Voltage. The cathode is on the left, where a negative high voltage is applied and the anode, on the right, is grounded. (c) Photograph of the plasma jet. Conditions : 80% N_2, I_d = 1.6 mA, P_1 = 30 mbar, P_2 = 10 mbar, gas flux = 36 sccm.

the plasma, from which the fluorescence is coming, can be approximated by a 14 μm diameter and 600 μm long cylinder.

2. *Fluorescence collection system*

Once excited by the laser, the N atom will de-excite emitting a fluorescence signal that is collected by means of a gated photomultiplier tube (PMT; Hamamatsu H11526-20-NF). The fluorescence is imaged onto a slit fixed in front of the PMT using a 10 cm-focal-length lens in a 4f configuration (see Fig. 2). A 600 μm horizontal slit limits the background noise and a band-pass filter selects the appropriate wavelength range of the fluorescence. This configuration allows for a better TALIF signal-to-noise ratio (SNR) to be achieved by limiting the background noise collected by the PMT. Because the size of the collection optic is much larger than that of the laser spot size, the spatial resolution of the technique is determined by the laser spot size.

To synchronize the laser pulse that induces the fluorescence with the gated PMT, the system is triggered using the visible part of the dye laser beam. It is directed onto a Thorlabs SM05PD2A photo-diode (PD1 in Fig. 2), which is connected to a Rohde & Schwartz RTO 1044 oscilloscope (4 GHz, 20 GS/s). The oscilloscope then produces a 1 ms signal, long enough to trigger a multi-function I/O device (National Instruments USB 6343, 1 MHz, 500 kS/s). This is used because the ns signal from the laser would have been too short. In turn, the device generates the triggers for the PMT. Taking in consideration the reponse time of all the devices and the length of the cables, the global response time of the system is of about 200 ns. This latter, in addition to the 1 ms signal mentionned before, impose that two laser pulses are necessary to perform TALIF measurements. The first pulse triggers the collection system and the second one generates the fluorescence signal that is actually recorded. The appropriate delay is thus imposed between the triggering laser shot and the 5 μs gate of the PMT.

The control of the whole platform, including the laser and collection system, as well as the signal acquisition and data processing, is done using a dedicated LabVIEW^{TM}program. For each measurement, by changing the laser frequency, we scan the absorption line around its central frequency (206.67 nm for nitrogen and 204.13 nm for krypton). At each laser frequency, we record the time-resolved fluorescence signal generated by the laser radiation at frequency ν_l, the laser pulse energy E_l, and the iodine fluorescence signal which is needed for wavelength calibration.

III. DETERMINATION OF THE ABSOLUTE N ATOM DENSITY USING NS-TALIF

A. N atoms density calibration using Krypton gas

To perform quantitative measurements of atomic densities using TALIF, a calibration technique using a noble gas, which was first introduced by Goehlich *et al*[28], has been widely used in the literature.

This method is based on the comparison of TALIF measurements performed in a noble gas with a known density, and those referring to an atomic species of interest. The TALIF excitation schemes of those two species must be as close as possible in terms of laser excitation and emitted fluorescence wavelengths. In this way, there is a negligible difference between the laser setup and fluorescence collection

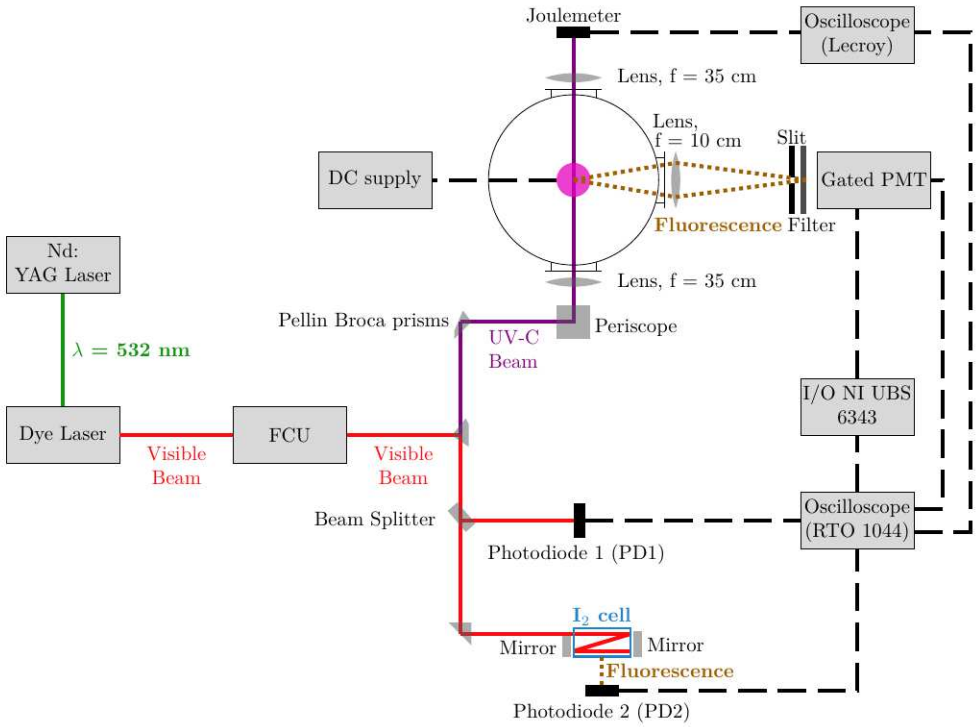

FIG. 2. Experimental set-up of the TALIF measurements. Solid lines represent laser radiation, dashed lines represent electric signals and dotted lines represent fluorescence emission. FCU : Frequency Conversion Unit.

optics between the two measurements. In the case of N atoms, Krypton (Kr) gas is well-suited and typically used for calibration purposes[29,30].

Figure 3 shows the two excitation schemes used for Kr and N. In the following, the ground states of nitrogen ($2p^3$) $^4S^0_{3/2}$ and krypton ($4p^6$) $^1S_0$ are referred to as N and Kr respectively, while the laser-excited states of nitrogen (3p) $^4S^0_{3/2}$ and krypton (5p') $[3/2]_2$ are denoted with N* and Kr* respectively. For nitrogen, the de-excitation to the states (2s) $^4P^0_{1/2;3/2;5/2}$ produces three fluorescence lines at 742.364, 744.230 and 746.831 nm that are all collected by the PMT. The de-excitation of Kr* to the state (5s) $[3/2]_1$ produces two lines at 587.09 nm and 826.32 nm, with a known ratio between them. We used the line at 587.09 nm to capture the fluorescence signal of Kr, since the 826.32 nm line may contain radiation emanating from other excited states. In the case where the laser-atom interaction is dominated by the two-photon absorption, the density of the N* (or Kr*) state is related to the offset frequency $\delta\nu_A = 2\nu_l - \nu_A$ where ν_l and ν_A are the laser central frequency and the absorption line central frequency for an atom A = N or Kr, respectively.

The relation between the known density of krypton n_{Kr} and the density of the ground state of atomic nitrogen n_N is the following[30]:

$$n_N = \frac{\eta_{Kr}}{\eta_N} \frac{T_{Kr} A_{Kr,5p\to5s}}{T_N \sum_{i=1}^{3} A_{N,i,3p\to3s}} \frac{\sigma^{(2)}_{Kr}}{\sigma^{(2)}_{N}} \frac{\tau_{Kr^*}}{\tau_{N^*}} \frac{\int_{\delta\nu_N=-\infty}^{\delta\nu_N=\infty} d\Psi_N}{\int_{\delta\nu_{Kr}=-\infty}^{\delta\nu_{Kr}=\infty} d\Psi_{Kr}} n_{Kr} \quad (1)$$

where η_{Kr} and η_N are the sensitivity of the PMT over the spectral range of the fluorescence signal of krypton and nitrogen respectively, T_{Kr} and T_N are the transmittance of the optics used for collecting the fluorescence signal of krypton and nitrogen respectively, $A_{Kr,5p\to5s}$ is the radiative decay rate (s^{-1}) for the Kr 5p $\to$ 5s transition measured, $A_{N,i,3p\to3s}$ is the radiative decay rate (s^{-1}) of the i^{th} radiative de-excitation process for the N 3p $\to$ 3s transition observed, $\sigma^{(2)}_{Kr}$ and $\sigma^{(2)}_{N}$ are the two-photon excitation cross-section (m^4) and τ_{Kr^*} and τ_{N^*} are the fluorescence decay times, i.e. the lifetimes of

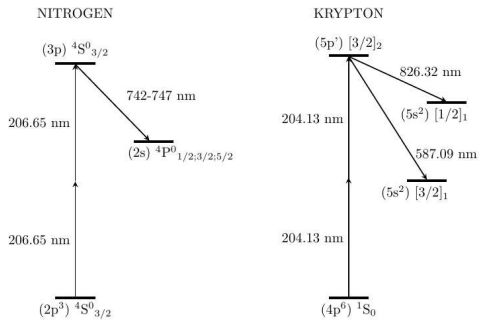

FIG. 3. Two-photon excitation and fluorescence scheme of nitrogen and krypton atom.

the Kr* and N* states, respectively, in the conditions of our experiments. $d\Psi_N$ and $d\Psi_{Kr}$ are the ratio number of detected fluorescence photons during dt to the square number of laser photons for a given laser central frequency ν_l (corresponding to an offset frequency $\delta\nu_A$). They are then integrated over the whole laser frequency domain.

Bisceglia *et al*[30] refer to equation 1 as the Full Excitation Method (FEM) since it requires recording the full line profile for each density measurement, which takes a significant amount of time (70 points are needed to properly resolve the line profile). To reduce the acquisition time, Bisceglia *et al*[30] suggest to experimentally determine the factor $g(\delta\nu_A)d(\delta\nu_A)$, $g(\delta\nu_A)$ being the statistical overlap factor between the atom absorption line and the normalized laser line. Thus, the product $g(\delta\nu_A)d(\delta\nu_A)$ represents the fraction of the laser energy that is actually used to excite the atoms, and its integral over the line is equal to 1. It depends on the line profiles of the laser and the absorption, which are both Gaussian in our case with full width at half maximum (FWHM) $\Delta\nu_l$ and $\Delta\nu_A$ respectively, and can be expressed by:

$$g(\delta\nu_A)d(\delta\nu_A) = \frac{d\Psi_A}{\int_{\delta\nu_A=-\infty}^{\delta\nu_A=\infty} d\Psi_A} = \frac{\sqrt{4\ln 2/\pi}}{\Delta\nu_A^{eff}} e^{-4\ln 2\left(\frac{\delta\nu_A}{\Delta\nu_A^{eff}}\right)^2} d(\nu_A) \quad (2)$$

where $\Delta\nu_A^{eff} = \sqrt{2\Delta\nu_l^2 + \Delta\nu_A^2}$ is the effective FWHM experimentally obtained from the line profile. We measured this effective FWHM over a wide range of plasma conditions and it was found to be of about 9.6 pm with a standard variation of only 0.8 pm. This is due to the fact that the effective broadening is largely dominated by the laser broadening, typically of 8 pm[30], which is much larger than what is reported in literature (1.06 pm in[31] and 1.53 pm in[32]).

This result means that we can accurately use the Peak Excitation Method (PEM) described by Bisceglia *et al*[30]. The full line profile and its integration $\int_{\delta\nu_A=-\infty}^{\delta\nu_A=\infty} d\Psi_A$ can be measured only once to determine the value of $g(\delta\nu_A)$. The density of N atoms can then be determined using a single laser shot at the central frequency ν_A, according to the equation[30]:

$$n_N = \frac{\eta_{Kr}}{\eta_N} \frac{T_{Kr} A_{Kr,5p\to5s}}{T_N \sum_{i=1}^{3} A_{N,i,3p\to3s}} \frac{\sigma_{Kr}^{(2)}}{\sigma_N^{(2)}} \frac{\tau_{Kr^*}}{\tau_{N^*}} \frac{d\Psi_N}{d\Psi_{Kr}} \frac{g(\delta\nu_{Kr})}{g(\delta\nu_N)} n_{Kr} \quad (3)$$

The calculation of the uncertainty on the density of nitrogen is done using the propagation of uncertainties of the independent variables[30,33]. In the following, this will be referred to as the total uncertainty. It takes into account all of the uncertainty sources, as calculated in[30]. The most significant uncertainty comes from the poor knowledge of the ratio of the two-photon absorption cross-sections $\sigma_{Kr}^{(2)}/\sigma_N^{(2)}$ which leads to an error of about 60% on the absolute density of the N atoms.

Nonetheless, it is worth noticing that the total uncertainty can be divided into two contributions: a systematic and a random uncertainty. Sources of a systematic error on the absolute density determination are the ratio of the two-photon absorption cross-sections mentioned above, the Einstein coefficients ($A_{Kr,5p\to5s}$ and $A_{N,i,3p\to3s}$), as well as the transmittance of the optics (T_{Kr} and T_N) and the sensitivity of the photomultiplier (η_{Kr} and η_N) for which the error is gathered from the manufacturer data-sheets. On the opposite, the TALIF integrals ($d\Psi_N$ and $d\Psi_{Kr}$), the fluorescence lifetimes (τ_{Kr^*} and τ_{N^*}) and the FWHM ($\Delta\nu_A$) used for the determination of $g(\delta\nu_A)$ are all sources of a random error. The repeatability of the discharge will also contribute to this random uncertainty on the measured density of N atoms. The random uncertainty can be estimated by repeating the same measurement several times. In this work, it is found to be of up to 30%, the worst cases being when the discharge is the most unstable and the density the lowest. In the following, it is referred as the repeatability uncertainty.

B. TALIF measurements validity verification

The hereinabove discussion and the validity of the equation (3) on the determination of the N atoms density, relies on the assumption that the laser-atom interaction is dominated by the two-photon laser absorption. Several phenomena can occur if the laser instantaneous and local power density is too high, such as photo-ionization, photo-dissociation and stimulated emission[27,34].

To make sure that these conditions are fulfilled, one can use the power dependence (PD) factor[35]. The PD factor is the slope obtained from the linear fit of the log-log plot of the integral of the TALIF signal versus the laser energy. When

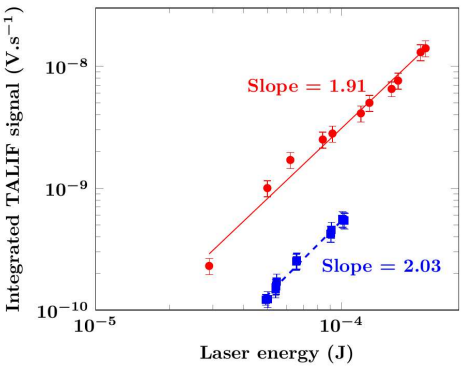

FIG. 4. Time-integrated TALIF signal as a function of the laser energy for Kr (red circles) and N (blue squares) along with associated linear fits. Error bars are obtained from the non-linear fitting procedure used to calculate the integral of the TALIF signal[30].

the two-photon laser absorption dominates over the other phenomena, the PD factor has a value of about 2.

In this work, we varied the laser energy using neutral density filters placed on the path of the laser beam, before the reactor, and measured the corresponding TALIF signal. Figure 4 shows the log-log plot of the integral of the TALIF signal as a function of the laser energy, for both Kr and N atoms. The corresponding linear fits are also plotted giving a PD factor of 1.91 for Kr and 2.03 for N. It shows that the laser-atoms interaction is dominated by the two-photon absorption and, thus, equation (3) can be used for the determination of the absolute density of N atoms in the discharge in this laser energy range.

C. Fluorescence lifetime and quenching rate

From equation (3), one can see that the precise knowledge of the radiative lifetimes τ_{Kr^*} and τ_{N^*} of the excited states Kr* and N* respectively, as well as the associated quenching coefficients, is critical for reliable quantitative measurements of the N atoms density. Some of the data are available in the literature referring to pure nitrogen environments, but the quenching coefficient of N* in an Ar/N_2 mixture is not measured, which motivated our study. The accurate measurement of the N atoms lifetime is limited by the duration of our laser pulse, which is 7 ns long. Indeed, TALIF measurements are difficult in conditions where the fluorescence lifetime is shorter than the laser pulse duration. In this case, the use of picosecond or femtosecond lasers can be a better solution[27,36,37].

For the krypton gas, we performed calibration measurements at a pressure of 1 mbar and measured a lifetime of 30.3 $\pm$ 1.8 ns. This value is higher than 28.5 ns, which is the one obtained when computing the Kr* radiative lifetime from the Einstein coefficient recommended by the NIST database[38], but lower than 34.1 ns[29], which is traditionally used in various TALIF diagnostics. At 1 mbar, we can thus consider the quenching of the Kr* atom to be negligible and the fluorescence decay time τ_{Kr^*} is equal to the radiative lifetime of the Kr* state.

For nitrogen atom, Figure 5 shows a typical fluorescence signal. Fitting the exponential decay of the PMT signal yields the time constant τ_{N^*} of the fluorescence decay, i.e. the decay of the population of the upper state N*.

The effective time constant for the fluorescence τ_{N^*} is a result of two factors:
- the natural radiative de-excitation of the excited level, with a time constant $\tau_{r,N^*} = \frac{1}{\sum_{i=1}^{3} A_{N,i,3p\rightarrow 3s}}$ where $A_{N,i,3p\rightarrow 3s}$ is the Einstein coefficient of the i^{th} radiative de-excitation process.
- the quenching rate Q of N* atoms by both N_2 molecules and Ar atoms.

Hence, the effective decay rate $1/\tau_{N^*}$ is expressed by:

$$\begin{aligned}\frac{1}{\tau_{N^*}} &= \frac{1}{\tau_{r,N^*}} + k_{q_{N_2}}[N_2] + k_{q_{Ar}}[Ar] \\ &= \frac{1}{\tau_{r,N^*}} + P \times \frac{10^{-4}}{k_B T} \times \left[k_{q_{N_2}} x_{N_2} + k_{q_{Ar}}(1 - x_{N_2})\right]\end{aligned} \quad (4)$$

where $k_{q_{N_2}}$ and $k_{q_{Ar}}$ are the quenching rates of N* by N_2 and Ar, respectively, in cm^3.s^{-1}, [N_2] and [Ar] are the densities of N_2 an Ar, respectively, in cm^{-3}, P is the pressure in mbar, k_B the Boltzmann constant in J.K^{-1}, T the gas temperature in K and x_{N_2} the fraction of N_2 in the gas mixture. τ_{N^*} and τ_{r,N^*} are expressed in s. Figure 6 shows the corresponding Stern-Volmer plots ($\frac{1}{\tau_{N^*}}$ in s^{-1} as a function of P in mbar) for different fractions of N_2 in the gas mixture (x_{N_2}).

The Stern-Volmer plot yields τ_{r,N^*} which is the inverse of the intercept in equation (4) for any gas mixture. Based on the results of Fig. 6, the radiative lifetime of N* is found equal to 26.4 $\pm$ 1.2 ns which is consistent with published values in the literature, e.g., 24.04 ns computed from the value of $A_{N,i,3p\rightarrow 3s}$ recommended by the NIST database[38], and 29.6 ns from[29]. Using our measurements at x_{N_2} = 1 in Fig. 6, we determined the quenching rate of N* by N_2, $k_{q_{N_2}}$ = 7.55 ($\pm$ 0.3) $\times 10^{-11}$ cm^3.s^{-1}, which is $\approx$1.8 and $\approx$1.1 times higher than the values of 4.1×10^{-11} cm^3.s^{-1} and 6.7×10^{-11} cm^3.s^{-1} reported in references[29] and[39] respectively. Finally, our experiments at x_{N_2} = 0.2 and 0.5 in Fig. 6 and another experiment performed at x_{N_2} = 0.8 (not presented in this paper) yield the quenching rate of N* by Ar, $k_{q_{Ar}}$ = 5.0 ($\pm$ 1.6) $\times 10^{-11}$ cm^3.s^{-1}. In contrast with $k_{q_{N_2}}$, we did not find any published value of $k_{q_{Ar}}$ in the literature to compare it with our result.
The lifetime measurements from Fig. 6 define the maximum pressure at which the absolute N atom density can be measured for each gas mixture. We chose to limit our measurements to effective lifetimes higher than 9 ns, in order to be

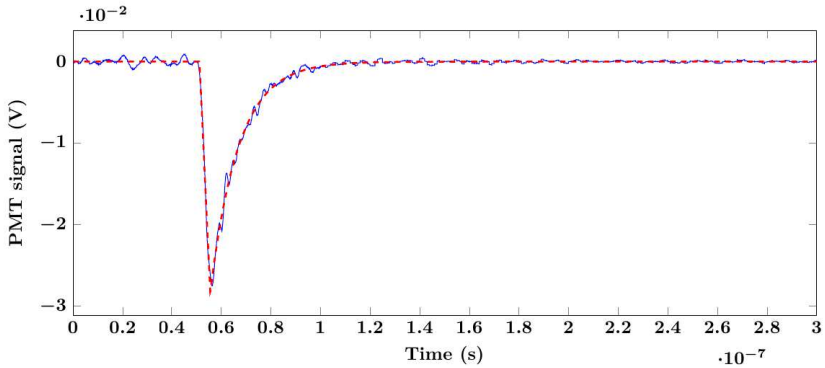

FIG. 5. Sample raw PMT signal (solid blue) in V as a function of time (s) and associated fit used to integrate the signal (dashed red). Plasma conditions : P = 50 mbar in both chambers, 80% N_2/20% Ar, I_d = 1 mA.

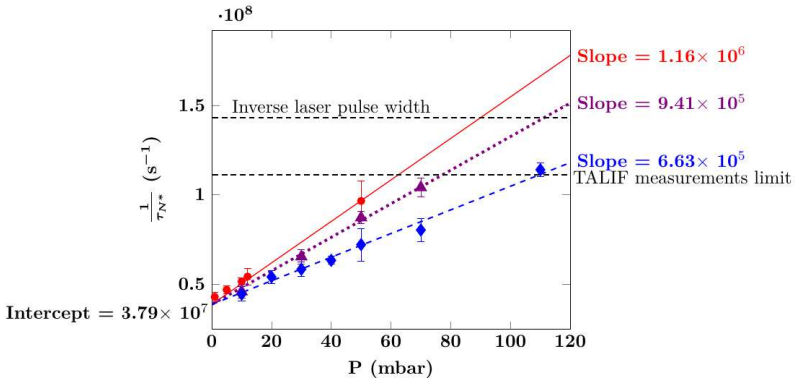

FIG. 6. Stern-Volmer plots of N* for different Ar/N_2 gas mixtures. Red circles : x_{N_2} = 1. Purple triangles : x_{N_2} = 0.5. Blue diamonds : x_{N_2} = 0.2 . The corresponding linear fits are plotted as well using solid red, dotted purple and dashed blue lines respectively. The upper dashed black horizontal line represents the inverse of the laser pulse width. The lower dashed black horizontal line represents the inverse of a 9 ns effective lifetime, which is the minimum lifetime for which TALIF measurements can be performed.

outside of the margin of error. The pressure limit then depends on the gas mixture as illustrated in Fig. 6: at 100% N_2, measurements can be made up to 65 mbar while at 20% N_2 the critical pressure increases up to 110 mbar.

IV. RESULTS AND DISCUSSION

For a clearer representation of our results, both the total and repeatability uncertainty can be considered in this paper. In section IV A, where we compare the absolute N atom density measured by two different techniques, the total uncertainty is used. However, for the rest of the results section, where we compare different TALIF measurements between them, the total uncertainty is less relevant since it is the same for every measurement. Thus, the repeatability uncertainty is used to better identify relevant trends.

A. Without pressure differential: Absorption spectroscopy and TALIF comparison

In this section, we compare the measurements of the N atoms density performed using TALIF (this work) and the high resolution Fourier Transform Spectrometer (FTS) in Vacuum Ultra Violet (VUV) of the DESIRS Beamline at SOLEIL synchrotron[40]. The latter results are reported by Remigy *et al.*[19]. Both works refer to the performance of parametric studies of the N atom density versus the gas mixture and pressure.

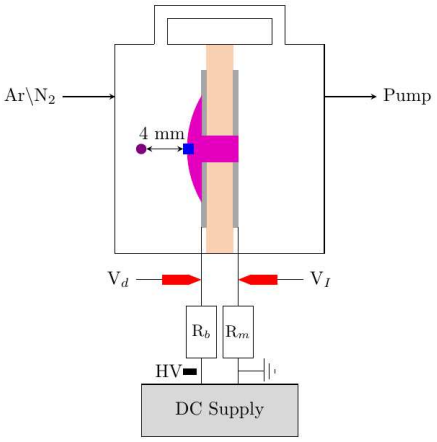

FIG. 7. Scheme of plasma configuration without a pressure differential between the two chambers indicating the location of the N atom density measurement by means of TALIF (purple circle) and FTS VUV (blue square).

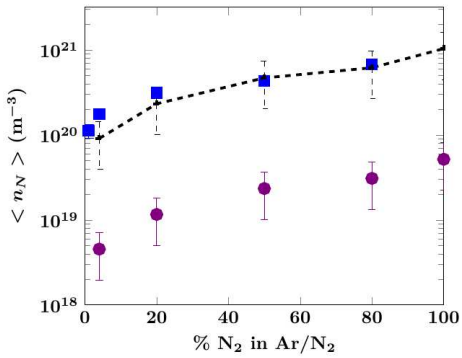

FIG. 8. Experimental densities of N atoms measured by FTS VUV (blue squares)[19] and TALIF (purple circles; this work) as a function of the percentage of N_2 in the Ar/N_2 gas mixture. The black dashed line represents the TALIF measurements corrected to take into account the fact that the two techniques are performed at different locations. Conditions: P = 50 mbar in both chambers, I_d = 1 mA. TALIF measurements are plotted with the total uncertainty.

For the measurements presented in this section, the valve is opened and both chambers are at the same pressure. Our experiments were focused on the cathodic side of the discharge, in front of the MHCD hole as illustrated in Figure 7. In Fig. 7, TALIF measurements are done 4 mm away from the plasma (purple circle) to avoid reflections of the laser radiation on the MHCD surface, while the FTS VUV measurements were performed at the cathodic expansion (blue square)[19].

1. *Influence of the gas mixture*

Figure 8 shows the densities of N atoms as a function of the percentage of N_2 into the Ar/N_2 gas mixture, measured with the TALIF method. FTS VUV measurements from[19] are plotted as well for comparison. With both methods, we note a similar trend: the N atoms density increases with the percentage of N_2, but not linearly as one would expect from the increase of N_2 concentration only. This trend can be explained by the fact that at low N_2 percentages, the electron density is high[19] while the electron temperature is only slightly lower than at higher N_2 percentages (2 eV at 50% N_2 compared to 1.5 eV at 0% N_2, i.e., pure Ar according to[41]) and can fairly efficiently dissociate the few present N_2 molecules (with a dissociation degree up to 1%). The electron - ion dissociative recombination reaction $N_2^+ + e \rightarrow N + N$ is the main production path of N atoms[19] because of the efficient charge transfer from the ion Ar^+ to N_2 ($Ar^+ + N_2 \rightarrow N_2^+ + Ar$)[42].
When the percentage of N_2 increases, the electron density drops as well as the dissociation rate. However, the N atoms density does not decrease because more N_2 is added and a decent dissociation rate is maintained thanks to the contribution of argon metastable atoms which can dissociate N_2 molecules[43].
Using TALIF, we were able to make one more measurement in a pure N_2 discharge, which was not possible by FTS VUV. The measured N atoms density was higher than those obtained in all Ar/N_2 mixtures. In pure nitrogen, it has been shown that the production of N atoms may occur through several processes which can be summed up in two categories: dissociation of the ground state molecules (at different vibrational levels, v) N_2 ($X^1\Sigma_g^+, v$) by electron impact, and collisions of N_2 molecules that are excited in various electronic and vibrational states[44]. While it is difficult to estimate the dominant dissociative processes in our case, since we are not aware of the existence of an extensive model of our peculiar discharge in nitrogen, it is possible that Ar atoms are not completely detrimental to a nitrogen discharge. This shall be further discussed in section IV B 3 hereafter.

From Fig. 8, although the trends obtained with the two techniques are very similar, we notice a great difference in the absolute value of the N atom density measured (more than one order of magnitude). It can be easily explained by the difference of the location at which the density is measured. Indeed, the N atoms density displays a profile which decreases with respect to the radial position r, according to the equation[19]:

$$n_N(r) = \frac{R_0 n_0}{r} \tag{5}$$

with R_0 the radius of the hole and n_0 the N atoms density at r = R_0 (blue square in Fig. 7). The FTS VUV measure-

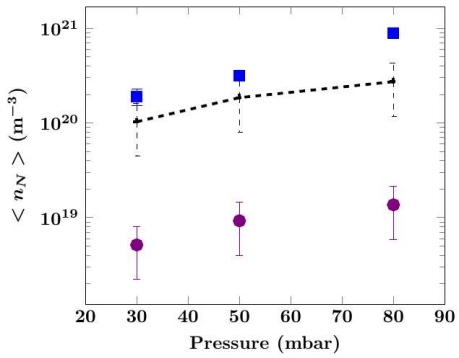

FIG. 9. Experimental densities of N atoms by FTS VUV (blue squares)[19] and TALIF (purple circles; this work) as a function of the pressure. The black dashed line represents the TALIF measurements corrected to take into account the fact that the two techniques are performed at different locations. Conditions: without pressure difference between the chambers, 20% N_2 in Ar/N_2, I_d = 1 mA. TALIF measurements are plotted with the total uncertainty.

ments estimate n_0 at R_0 = 0.2 mm. Using equation (5), we can estimate this density as well from the density measured by TALIF at r = 4 mm, as follows: $n_0(TALIF) = n_N$(r = 4 mm) × (4 mm / 0.2 mm). This estimation has been plotted in Fig. 8 with a dashed line and it matches very well the FTS VUV measurements.

2. *Influence of the pressure*

Figure 9 illustrates the density of N atoms as a function of the gas pressure, measured with TALIF (purple circles) and FTS VUV (blue squares). The density $n_0(TALIF)$, estimated as explained before, is plotted with a dashed line. As it can be seen, it matches well the FTS VUV measurements, although a discrepancy exists for a pressure of 80 mbar. This could be due to the fact that the discharge is less stable at higher pressure and the FTS VUV measurement at 80 mbar was only done once, and is thus less reliable.

Nevertheless, the evolution of the N atoms density with the pressure is similar with both techniques and the density increases with an increased pressure. This trend shows that the production process of N atoms varies with the pressure as it was shown using a 0D (volume-averaged) global model of the discharge[19]. It is mostly due to the increased contribution from the metastable pooling dissociation reaction $N_2(A^3\Sigma_u^+)$ + $N_2(A^3\Sigma_u^+) \rightarrow N_2\ (X^1\Sigma_g^+)$ + N + N. Based on other studies, it seems that this process becomes more and more significant when the pressure is increased, for example, from 20 to 200 mtorr in an ICP discharge[42].

B. With pressure differential: TALIF measurements of the N atoms density in a MHCD jet

In this section, we present the measurements performed with a pressure differential between the two chambers, i.e., using the configuration of Fig. **??**b where the valve between the two chambers is closed. For simplicity, the pressure in the high pressure (upstream) chamber is denoted P_1 and that in the low pressure (downstream) chamber, where a plasma jet is formed, is denoted P_2 ($P_1 > P_2$). The cathode of the MHCD is found in the high pressure chamber, while the anode in the low pressure chamber. The position of the TALIF measurements is located based on the coordinate system of Fig. **??**b.

1. *Spatial mapping*

Figure 10 shows the evolution of the N atoms density as a function of the axial (y) and radial (x) position in the downstream chamber. In Fig.10, the density of N atoms remains almost constant along the jet axis: it decreases by only 16% over 35 mm. Fig.10 shows however that the density drops as we move away from the jet axis (x = 0), being two times lower at x = 20 mm. This decrease could be overcome using an array of holes, with MHCDs working in parallel[21]. In comparison with the case of a MHCD without a jet, we can see that there are N atoms over a long distance along the jet axis. It is unlikely that N atoms are produced directly inside the jet. Indeed, the structure of the electric field is peculiar in the MHCD[45]. The potential difference is mainly localized in the annular cathode sheath involving a strong radial electric field (along the axis $\vec{x}$ illustrated in Fig.1) in this region. The electrons emitted at the cathode are accelerated in the cathode sheath by this strong electric field. Out of this region, in the so-called positive column, the electric field lines are found on the axial direction (along the axis $\vec{y}$ illustrated in Fig.1) having a much weaker magnitude. Thus, the electrons are accelerated from the cathodic region to the anode where they are collected. The motion of the electrons is induced by the electric force and not by the pressure gradient which drastically decreases the possibility to have electrons outside of the hole on the anodic side in our configuration. Hence, it is most likely that the N atoms are produced in the cathodic region, where most the electric power is deposited[46] and then either diffuse in the cathodic chamber (in the case where there is no pressure differential), or are transported along the anodic chamber due to the pressure differential. This is especially interesting for atomic nitrogen deposition purposes: the N atoms are produced inside the MHCD hole, which, besides the fact that it is very compact (only 1 mm long), allows for a transport of active species over several centimeters in the downstream chamber. It should be noted that due to the small diameter of the reactor window, we were not able to perform more measurements along the jet axis.

The N atoms losses in the volume, in an Ar/N_2 mixture, originate in three-body collisions with Ar atoms and N_2 molecules. The reaction rates of these reactions $(8.27 \times 10^{-34} \times \exp(500/T_g(K))$ cm^6s^{-1} for N_2 and half as

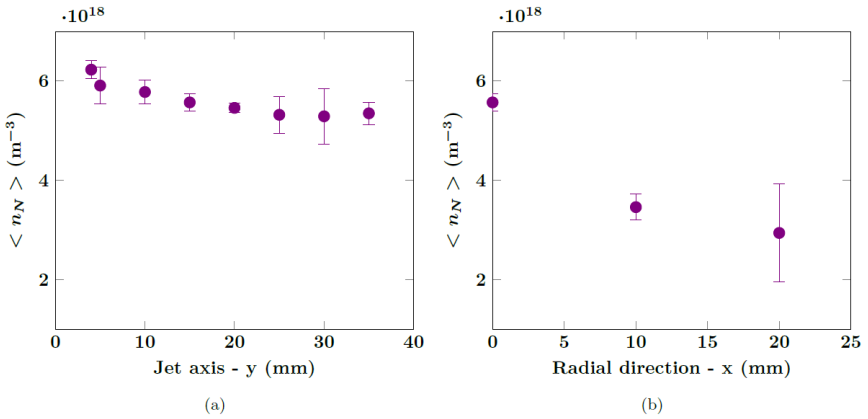

FIG. 10. Experimental densities of N atoms as a function of the position (a) along the jet axis $\vec{y}$, on the hole axis of symmetry (x = 0 mm) and (b) along the radial direction $\vec{x}$, at y = 15 mm. 20% N_2 in Ar/N_2, I_d = 1.6 mA, P_1 = 50 mbar, P_2 = 1 mbar, gas flux = 40 sccm. Data points are plotted with the repeatability uncertainty.

much for Ar[43]; T_g is the gas temperature) being very small, with a resulting lifetime of about 1 minute, the N atoms losses in the volume can be neglected. Thus, we expect the diffusion profile of N atoms to be resulting from fluid phenomena and the decrease of the N atoms density measured along the $\vec{y}$ axis can likely be explained by the mixing of the plasma jet with the ambient gas in the low pressure chamber.

For this reason, and a clearer study of the influence of other parameters on the production of N atoms, only the measurements performed at x = 0 and y = 4 mm are presented in the following.

2. *Effect of the discharge current*

Figure 11 depicts the evolution of the N atoms density as a function of the discharge current. The density increases by about 30% with a discharge current increases from 1 to 2 mA. For a MHCD working in the normal regime, the discharge voltage is constant, even if the discharge current increases[47,48]. The increase of the discharge current will also induce an increase of the surface of the cathodic expansion, to provide the additional electrons needed. These two phenomena, the increase of the discharge current and the increase of the cathodic expansion surface have opposite effects on the current density. Indeed, the ratio of the discharge current to the surface on which it is collected, involves an almost constant current density[49]. The limited effect of the discharge current on the electron density has been measured previously in a similar discharge in pure argon[49]. This explain the slight effect on the density of excited species, such as N atoms, which is shown in Fig. 11.

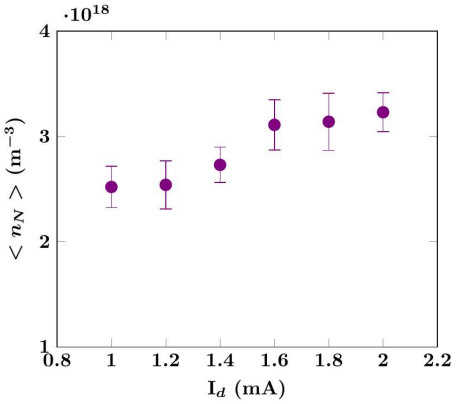

FIG. 11. Experimental densities of N atoms as a function of the discharge current. 10% N_2 in Ar/N_2, P_1 = 50 mbar, P_2 = 1 mbar, gas flux = 100 sccm. Plotted with the repeatability uncertainty.

3. *Effect of the gas mixture*

Figure 12 shows the evolution of the N atoms density in the plasma jet as a function of the gas mixture. The density increases sharply as the N_2 percentage in the gas mixture increases from 10 to 20% and then increases slower between 20 and 80 % of N_2. A maximum density seems to be reached around 95 % of N_2 before going slightly down at 100% N_2 (i.e., pure nitrogen discharge).
We notice that this tendency is the same as the one measured without a pressure differential in section IV A 1, suggesting

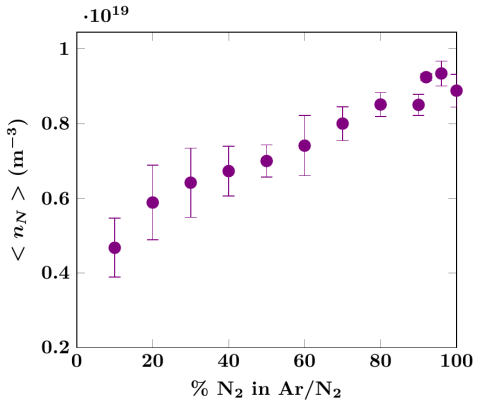

FIG. 12. Experimental densities of N atoms as a function of the percentage of N_2 in the Ar/N_2 gas mixture. I_d = 1.6 mA, P_1 = 50 mbar, P_2 = 1 mbar, gas flux = 100 sccm. Data points are plotted with the repeatability uncertainty.

that the chemistry involved is very similar. Indeed, as discussed in section IV B 1, the production of excited species seems to happen very similarly inside the hole in both cases, and only the way they are transported to the location of the measurement differs.

The supplementary data obtained here at high N_2 percentages, between 90 % and 100 %, reveal a maximum which may indicate that there are some advantages of adding small argon admixtures in a nitrogen discharge, although their effect on the N atom density increase is moderate. At higher pressures, electronically excited states of N_2 start playing an important role. For instance, the metastable pooling dissociation reaction $N_2(A^3\Sigma_u^+) + N_2(A^3\Sigma_u^+) \rightarrow N_2\ (X^1\Sigma_g^+) + N + N$ has been shown to gain in importance[19,42], although it is not a very efficient source of N atoms. The kinetics of the $N_2(A^3\Sigma_u^+)$ and the other electronically excited states $N_2\ (B^3\Pi_g)$ and $N_2\ (C^3\Pi_u)$ was shown to be coupled in a collisional-radiative loop with main exit channels producing vibrational states of N_2[30,50]. Vibrational states and the vibrational ladder phenomena are known to be a significant production channel for N atoms in pure N_2 discharge[51].

This phenomenon may still be significant in nitrogen plasmas with small amounts of argon. When added in small admixtures, Ar atoms may produce electronic states such as $N_2\ (A^3\Sigma_u^+)$[52], $N_2\ (B^3\Pi_g)$ and especially $N_2\ (C^3\Pi_u)$[53], fueling the collisional-radiative loop mentioned before. This loop may then lead to the production of vibrational states of N_2 followed by production of N atoms.

Another production channel that argon addition may enhance is the electron-ion dissociative recombination reaction, i.e. $N_2^+ + e \rightarrow N + N$. Indeed, the ion charge transfer $Ar^+ + N_2 \rightarrow N_2^+ + Ar$ is very efficient[54] and an increase in the N_2^+ density could translate in an increased production of N atoms. In the literature, it was also found that argon admixture has a limited impact on the electronic temperature in the discharge[55] and, thus, will not negatively impact the efficiency of the electron-ion dissociative recombination reaction.

Finally, argon admixture also allows for the discharge to be operated at a lower injected power.

Even though the evolution of the N atoms density with the percentage of N_2 is similar with and without a pressure differential, we notice a great discrepancy in the absolute density of N atoms measured. Given that the cathodic region is the place where most of the power is deposited, hence where excited species are produced, one may think that the pressure on the cathodic side will be the one impacting the production in the hole, even with a pressure differential. We, thus, compared results without a pressure differential at 50 mbar in both chambers, and results with a pressure differential at 50 mbar in the cathodic chamber (P_1 = 50 mbar). With the same current and same gas mixture, the density measured in the jet (P_1 = 50 mbar and P_2 = 1 mbar), is about 60 times lower than that estimated in the cathodic region without the jet (both chambers at P = 50 mbar). For instance, at 1 mA, 10% N_2, P = 50 mbar, the density on the cathodic side, without a jet, inside the hole is around 1.5×10^{20} m^{-3} (see Fig. 8) while it is of 2.5×10^{18} m^{-3} inside the jet (see Fig. 11). This difference can be partially explained by the transport of the plasma and mixing with surrounding gas when entering the low pressure chamber. The recombination of N atoms on the walls of the hole could be another explanation, as well as the fact that the gas spends less time in the cathodic region.

In the next two sections, we explore the influence of the pressures: (i) the lower pressure P_2, in the chamber where the jet is formed, and (ii) the higher pressure P_1, at the cathodic side of the MHCD.

4. *Effect of the lower pressure*

Figure 13 shows the evolution of the N atoms density as a function of the lower pressure P_2. The upper pressure is fixed at P_1 = 50 mbar; the gas flux injected and the strength of the pumping are adapted to obtain different pressures P_2. The density of N atoms, measured 4 mm downstream of the MHCD in the jet, is 4 times higher when P_2 is increased by a factor of 10. This could be due to the fact that the higher P_2 is the more time the gas mixture spends in the cathodic region where excited species are created.

5. *Effect of the higher pressure*

Figure 14 shows the evolution of the N atoms density as a function of the higher pressure P_1. The lower pressure is fixed at P_2 = 2 mbar; the gas flux injected and the strength of the pumping are adapted to obtain different pressures P_1. The density of N atoms, measured 4 mm downstream of the MHCD in the jet, is decreasing when P_1 increases. However, the density value is a lot less sensitive to variations of P_1 than it is to variations of P_2: the density only decreases by 30%

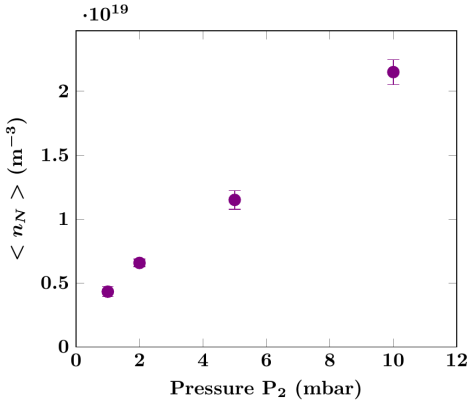

FIG. 13. Experimental densities of N atoms as a function of the gas pressure in the low pressure chamber. 100% N_2, I_d = 1.6 mA, P_1 = 50 mbar, gas flux and strength of the pumping adapted to regulate the pressure (between 34 and 36 sccm). Data points are plotted with the repeatability uncertainty.

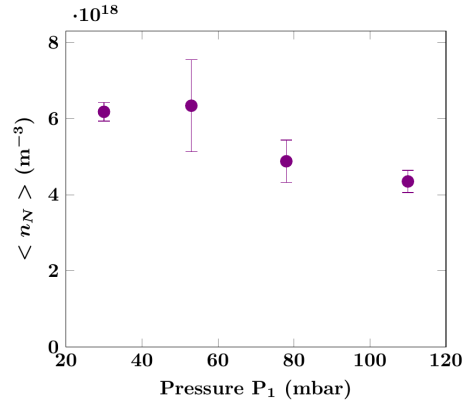

FIG. 14. Experimental densities of N atoms as a function of the gas pressure in the high pressure chamber. 100% N_2, I_d = 1.6 mA, P_2 = 2 mbar, gas flux and strength of the pumping adapted to regulate the pressure (between 20 and 80 sccm). Data points are plotted with the repeatability uncertainty.

over a range of pressure of 80 mbar. The same kind of phenomena could explain the evolution of the N atoms density as a function of P_1 and P_2, since in both cases, the density decreases when the pressure differential ($\Delta P = P_1 - P_2$) increases.

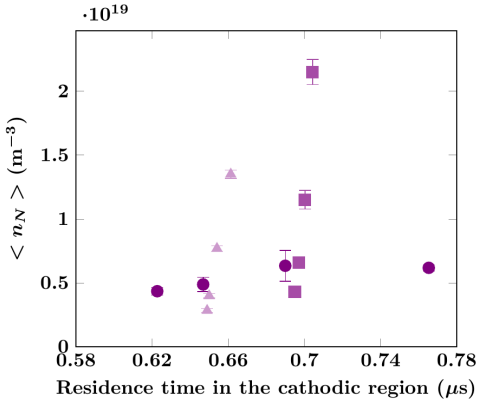

FIG. 15. Experimental densities of N atoms as a function of the residence time in the cathodic region. Circles are with P_2 = 2 mbar and P_1 varying. Squares are with P_1 = 50 mbar and P_2 varying. Triangles are with P_1 = 70 mbar and P_2 varying. 100% N_2, I_d = 1.6 mA, P_1 = 30-110 mbar, P_2 = 1-10 mbar, gas flux and strength of the pumping adapted to regulate the pressures. Data points are plotted with the repeatability uncertainty.

6. N atoms density as a function of the residence time in the cathodic region

As discussed in the previous sections, the dominant phenomenon which could explain the different trends of the measured N atom density might be the residence time in the cathodic region, which varies with ΔP, and would prevent the plasma from reaching the stationary regime before it is thrust outside the cathodic region. Using the commercial software Ansys Fluent™, we were able to perform Computational Fluid Dynamics (CFD) simulation, i.e. without plasma, and compute the velocity profile of the gas inside the hole and estimate its residence time in the cathodic region (100 μm long). Measurements from sections IV B 4 and IV B 5 are then plotted as a function of this parameter.

Figure 15 shows the N atoms density as a function of the gas residence time in the cathodic region. We first notice that there is no general correlation of the density variation with the residence time. To try to elucidate the role of the residence time, we plotted with different symbols, three groups of measurements performed with one of the two pressures constant, the other being variable.
Circles are measurements referring to P_2 = 2 mbar (constant) and P_1 variable from 30 to 110 mbar. Although P_1 variation has a great incidence on the residence time, we notice that the effect on the N atoms density is small, with a slight density increase between a residence time of 0.62 and 0.77 μs. Squares and triangles represent groups of measurements performed at P_1 = 50 mbar and P_1 = 70 mbar, respectively, while varying P_2 from 1 to 10 mbar. We observe that although

the change of P_2 has a very small impact on the residence time, its effect on the N atoms density production is much larger when compared to that of P_1.

The role of the residence time seems to be negligible even if for a constant P_2 (circles in Fig. 15) its influence is probably compensated by an increased N atom production at higher pressures in the cathodic region[19], which could compensate the decrease of the density at lower residence times. In the literature, MHCD jets are usually operated at atmospheric pressure[56] and in most cases the jet moves out of the cathodic side of the MHCD[57,58]. Furthermore, MHCD setups driven by pulsed power supplies can be found[59]. In these conditions, the pressure on the two sides of the MHCD cannot be controlled independently as it is the case in our configuration. With the lower pressure put equal to the atmospheric one, the analog to a variation of the higher pressure is a change of the gas flux. However, this only corresponds to a variation of the higher pressure P_1 and we did not find in literature a jet where the lower pressure can be varied. Giuliani et al.[59] showed that turbulences in the plasma plume highly influence the plasma inside the hole due to the cooling of the gas, which was also suggested by Pei et al.[56]. This could also be happening in our conditions, with the pressure P_2 having a larger influence on the jet turbulences than the pressure P_1, thus having a higher impact on the N atoms density. These pressures may also have an impact on the N atoms recombination in the hole, and hence on their density in the plume.

V. CONCLUSION

Measurements of the N atom density in a MHCD operated in an Ar/N_2 gas mixture have been performed using the TALIF technique.

First, with the MHCD operating with the same gas pressure on both sides (chambers), we reproduced a previous study conducted using VUV absorption spectroscopy. The results of the two techniques are very coherent, with differences that can be easily explained with a simple diffusion model.

The end target of our group being to be able to use the MHCD as a nitrogen source for deposition processes, a pressure differential was introduced between the two sides of the MHCD. It creates a plasma jet towards the lower pressure chamber, which can transport N atoms relatively over long distances (few centimeters), while the region in which they are initially created is only 1 mm long. A study of the influence of the percentages of Ar and N_2 in the gas mixture showed that a few percent of argon admixed in a nitrogen can very slightly increase the density of N atoms produced (an increase of 5% of the density is measured when 4% of Ar is added, compared to pure nitrogen). The chemistry involved is similar to the case without the plasma jet. The optimum conditions to maximize the density of N atoms produced are with a gas mixture of 96% N_2 and 4% of argon admixture, a pressure in the high pressure chamber of 30 mbar and 10 mbar in the low pressure chamber.

The generation of the jet seems to have effects that are linked to fluid dynamics. We studied the influence of the pressure variation on both sides of the MHCD: the lower pressure P_2 has a much more distinct effect on the density of N atoms measured 4 mm downstream of the hole on its axis. On the opposite, the effect of the higher pressure P_1 is rather small. This difference on the impact of the two pressures is probably related to three main phenomena: (i) the modification of the time spent in the cathodic region where most of the power is deposited, (ii) the recombination of N atoms on the sides of the hole and (iii) the turbulences in the plasma jet.

ACKNOWLEDGMENTS

This work is supported by the French Research National Agency (ANR) through the DESYNIB project (ANR-16-CE08-0004 JCJC). The authors would like to thank Gérard Bauville for the fabrication of the MHCD devices used for this study. ....

DATA AVAILABILITY STATEMENT

The data that support the findings of this study are available within the article.

[1]W. C. Hughes, W. H. R. Jr, M. a. L. Johnson, S. Fujita, J. W. C. Jr, J. F. Schetzina, J. Ren, and J. A. Edmond, Journal of Vacuum Science & Technology B: Microelectronics and Nanometer Structures Processing, Measurement, and Phenomena **13**, 1071–1023 (1998).
[2]M. Park, J. Min, J. Lee, H. Hwang, C. Kim, S. Kang, C. Kang, J. Park, Y. Jho, and D. Lee, Journal of Crystal Growth **528**, 125233 (2019).
[3]M. Siekacz, M. Sawicka, H. Turski, G. Cywiński, A. Khachapuridze, P. Perlin, T. Suski, M. Boćkowski, J. Smalc-Koziorowska, M. Kryśko, R. Kudrawiec, M. Syperek, J. Misiewicz, Z. Wasilewski, S. Porowski, and C. Skierbiszewski, J. Appl. Phys. **110**, 063110 (2011).
[4]D. Li, K. Jiang, X. Sun, and C. Guo, Advances in Optics and Photonics **10**, 43–110 (2018).
[5]Q. Z. Liu and S. S. Lau, Solid-State Electronics **42**, 677–691 (1998).
[6]J. Achard, V. Jacques, and A. Tallaire, J. Phys. D: Appl. Phys. **53**, 313001 (2020).
[7]J. Wang, F. Ma, and M. Sun, RSC Advances **7**, 16801–16822 (2017).
[8]C. R. Dean, A. F. Young, I. Meric, C. Lee, L. Wang, S. Sorgenfrei, K. Watanabe, T. Taniguchi, P. Kim, K. L. Shepard, and J. Hone, Nature Nanotechnology **5**, 722–726 (2010).
[9]A. Tallaire, O. Brinza, P. Huillery, T. Delord, C. Pellet-Mary, R. Staacke, B. Abel, S. Pezzagna, J. Meijer, N. Touati, L. Binet, A. Ferrier, P. Goldner, G. Hetet, and J. Achard, Carbon **170**, 421–429 (2020).
[10]J. Engelhardt, G. Hahn, and B. Terheiden, Energy Procedia **77**, 786–790 (2015).
[11]F. Silie, C. Junfang, G. Peng, and W. Chun-ann, Vacuum **86**, 1517–1521 (2012).
[12]M. Singh, H. Vasudev, and R. Kumar, Materials Today: Proceedings **26**, 2277–2282 (2020).
[13]K. H. Schoenbach and K. Becker, The European Physical Journal D **70**, 29 (2016).
[14]L. Lin and Q. Wang, Plasma Chemistry and Plasma Processing **35**, 925–962 (2015).
[15]K. H. Schoenbach, R. Verhappen, T. Tessnow, F. E. Peterkin, and W. W. Byszewski, Appl. Phys. Lett. **35**, 925–962 (1996).
[16]X. Aubert, G. Bauville, J. Guillon, B. Lacour, V. Puech, and A. Rousseau, Plasma Sources Sci. Technol. **16**, 23–32 (2007).
[17]C. Lazzaroni, P. Chabert, A. Rousseau, and N. Sadeghi, The European Physical Journal D **60**, 555–563 (2010).
[18]C. Lazzaroni and P. Chabert, J. Appl. Phys. **111**, 053305 (2012).

[19]A. Remigy, S. Kasri, T. Darny, H. Kabbara, L. William, G. Bauville, K. Gazeli, S. Pasquiers, J. Santos Sousa, N. De Oliveira, N. Sadeghi, G. Lombardi, and C. Lazzaroni, J. Phys. D: Appl. Phys. **55**, 105202 (2022).
[20]A.-A. Mohamed, J. F. Kolb, and K. H. Schoenbach, The European Physical Journal D **60**, 517–522 (2010).
[21]S. Kasri, L. William, X. Aubert, G. Lombardi, A. Tallaire, J. Achard, C. Lazzaroni, G. Bauville, M. Fleury, K. Gazeli, S. Pasquiers, and J. S. Sousa, Plasma Sources Sci. Technol. **28**, 035003 (2019).
[22]J. S. Sousa, G. Bauville, B. Lacour, V. Puech, M. Touzeau, and L. C. Pitchford, Appl. Phys. Lett. **93**, 011502 (2008).
[23]S. He, X. Zhang, J. Ha, J. Li, P. Wang, and Q. Li, Physics of Plasmas **27**, 102108 (2020).
[24]H. Kabbara, S. Kasri, O. Brinza, G. Bauville, K. Gazeli, J. Santos Sousa, V. Mille, A. Tallaire, G. Lombardi, and C. Lazzaroni, Appl. Phys. Lett. **116**, 171902 (2020).
[25]C. Dumitrache, A. Gallant, N. d. Oliveira, C. O. Laux, and G. D. Stancu, Plasma Sources Sci. Technol. **31**, 015004 (2022).
[26]E. Es-sebbar, Y. Benilan, A. Jolly, and M.-C. Gazeau, J. Phys. D: Appl. Phys. **42**, 135206 (2009).
[27]G. D. Stancu, Plasma Sources Sci. Technol. **29**, 054001 (2020).
[28]A. Goehlich, T. Kawetzki, and H. F. Döbele, J. Chem. Phys. **108**, 9362 (1998).
[29]K. Niemi, V. S.-v. d. Gathen, and H. F. Döbele, J. Phys. D: Appl. Phys. **34**, 2330–2335 (2001).
[30]E. Bisceglia, S. Prasanna, K. Gazeli, X. Aubert, C. Y. Duluard, G. Lombardi, and K. Hassouni, Plasma Sources Sci. Technol. **30**, 095001 (2021).
[31]S. Mazouffre, C. Foissac, P. Supiot, P. Vankan, R. Engeln, D. C. Schram, and N. Sadeghi, Plasma Sources Sci. Technol. **10**, 168–175 (2001).
[32]E. Es-Sebbar, C. Sarra-Bournet, N. Naudé, F. Massines, and N. Gherardi, J. Appl. Phys. **106**, 073302 (2009).
[33]S. P. Venkateshan, *Mechanical Measurements* (John Wiley & Sons, 2015).
[34]H. F. Döbele, T. Mosbach, K. Niemi, and V. S.-v. d. Gathen, Plasma Sources Sci. Technol. **14**, S31–S41 (2005).
[35]S. Agrup, F. Ossler, and M. Aldén, Applied Physics B Lasers and Optics **61**, 479–487 (1995).
[36]K. Gazeli, X. Aubert, S. Prasanna, C. Y. Duluard, G. Lombardi, and K. Hassouni, Physics of Plasmas **28**, 043301 (2021).
[37]K. Gazeli, G. Lombardi, X. Aubert, C. Y. Duluard, S. Prasanna, and K. Hassouni, Plasma **4**, 145–171 (2021).
[38]A. Kramida, Y. Ralchenko, J. Reader, and N. A. Team, Published: NIST Atomic Spectra Database (ver. 5.9), [Online]. Available: https://physics.nist.gov/asd [2022, January 20]. National Institute of Standards and Technology, Gaithersburg, MD.
[39]S. F. Adams and T. A. Miller, Chemical Physics Letters **295**, 305–311 (1998).
[40]N. de Oliveira, D. Joyeux, D. Phalippou, J. C. Rodier, F. Polack, M. Vervloet, and L. Nahon, Rev. Sci. Instrum. **80**, 043101 (2009).
[41]S. Kasri, *Développement de sources microplasma en mélange N_2/Ar pour la production d'azote atomique en vue d'une application aux procédés de dépôt de nitrure.*, PhD dissertation, Université Sorbonne Paris Cité (2019), https://tel.archives-ouvertes.fr/tel-03180054.
[42]N. Kang, F. Gaboriau, S. Oh, and A. Ricard, Plasma Sources Sci. Technol. **20**, 045015 (2011).
[43]A. Bogaerts, Spectrochimica Acta Part B: Atomic Spectroscopy **64**, 126–140 (2009).
[44]A. V. Volynets, D. V. Lopaev, T. V. Rakhimova, A. A. Chukalovsky, Y. A. Mankelevich, N. A. Popov, A. I. Zotovich, and A. T. Rakhimov, J. Phys. D: Appl. Phys. **51**, 364002 (2018).
[45]C. Lazzaroni and P. Chabert, J. Phys. D: Appl. Phys. **46**, 455203 (2013).
[46]C. Lazzaroni and P. Chabert, J. Phys. D: Appl. Phys. **44**, 445202 (2011).
[47]K. H. Schoenbach, A. El-Habachi, W. Shi, and M. Ciocca, Plasma Sources Sci. Technol. **6**, 468 (1997).
[48]A. Rousseau and X. Aubert, J. Phys. D: Appl. Phys. **39**, 1619–1622 (2006).
[49]C. Lazzaroni, *Etude théorique et expérimentale d'une micro décharge à cathode creuse à pression intermédiaire dans l'argon.*, PhD dissertation, Ecole Polytechnique X (2010), https://pastel.archives-ouvertes.fr/pastel-00552043.
[50]V. Guerra and J. Loureiro, Plasma Sources Sci. Technol. **6**, 361–372 (1997).
[51]M. Capitelli, G. Colonna, G. D'Ammando, V. Laporta, and A. Laricchiuta, Chemical Physics **438**, 31–36 (2014).
[52]J. Henriques, E. Tatarova, V. Guerra, and C. Ferreira, Vacuum **69**, 177–181 (2002).
[53]M. Touzeau and D. Pagnon, Chemical Physics Letters **53**, 355–360 (1978).
[54]Y. A. Lebedev, T. B. Mavludov, I. L. Epstein, A. V. Chvyreva, and A. V. Tatarinov, Plasma Sources Sci. Technol. **21**, 015015 (2012).
[55]J. Ma and Y.-K. Pu, Physics of Plasmas **10**, 4118–4122 (2003).
[56]X. Pei, J. Kredl, X. Lu, and J. F. Kolb, J. Phys. D: Appl. Phys. **51**, 384001 (2018).
[57]Z. Duan, P. Li, F. He, R. Han, and J. Ouyang, Plasma Sources Sci. Technol. **30**, 025001 (2021).
[58]B. N. Sismanoglu, K. G. Grigorov, R. Caetano, M. V. Rezende, and Y. D. Hoyer, The European Physical Journal D **60**, 505–516 (2010).
[59]L. Giuliani, M. Xaubet, D. Grondona, F. Minotti, and H. Kelly, Physics of Plasmas **20**, 063505 (2013).
[60]I. Armenise, M. Capitelli, E. Garcia, C. Gorse, A. Laganà, and S. Longo, Chemical Physics Letters **200**, 597–604 (1992).
[61]V. Guerra, P. A. Sá, and J. Loureiro, European Physical Journal Applied Physics **28**, 125–152 (2004).
[62]N. A. Popov, Plasma Physics Reports **39**, 420—-424 (2013).
[63]T. L. Chng, N. D. Lepikhin, I. S. Orel, N. A. Popov, and S. M. Starikovskaia, Plasma Sources Sci. Technol. **29**, 035017 (2020).

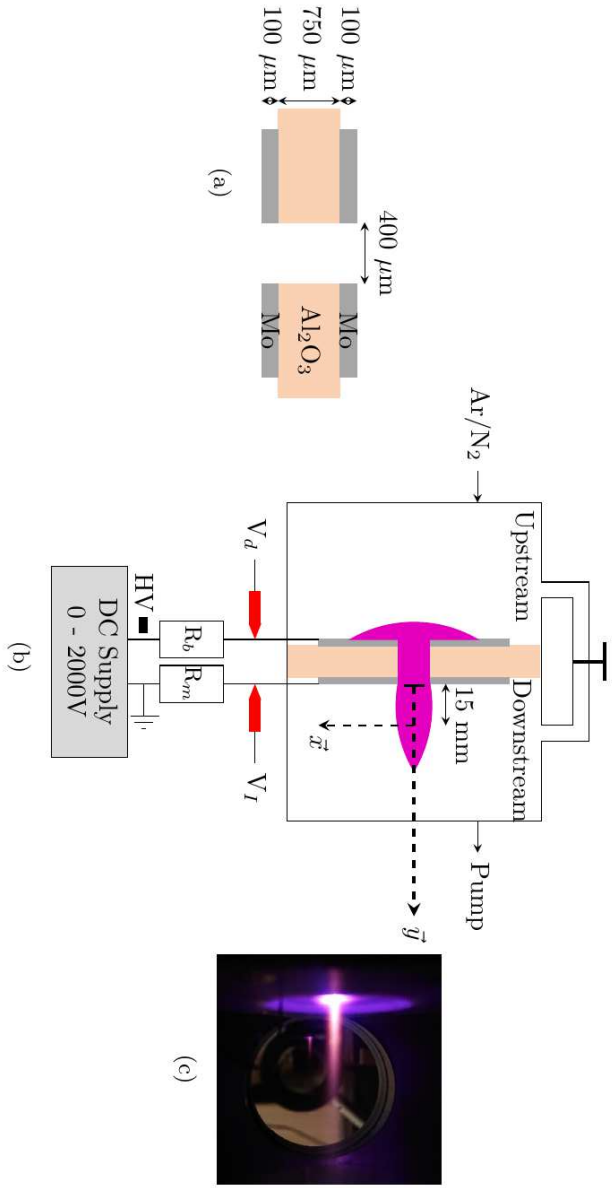

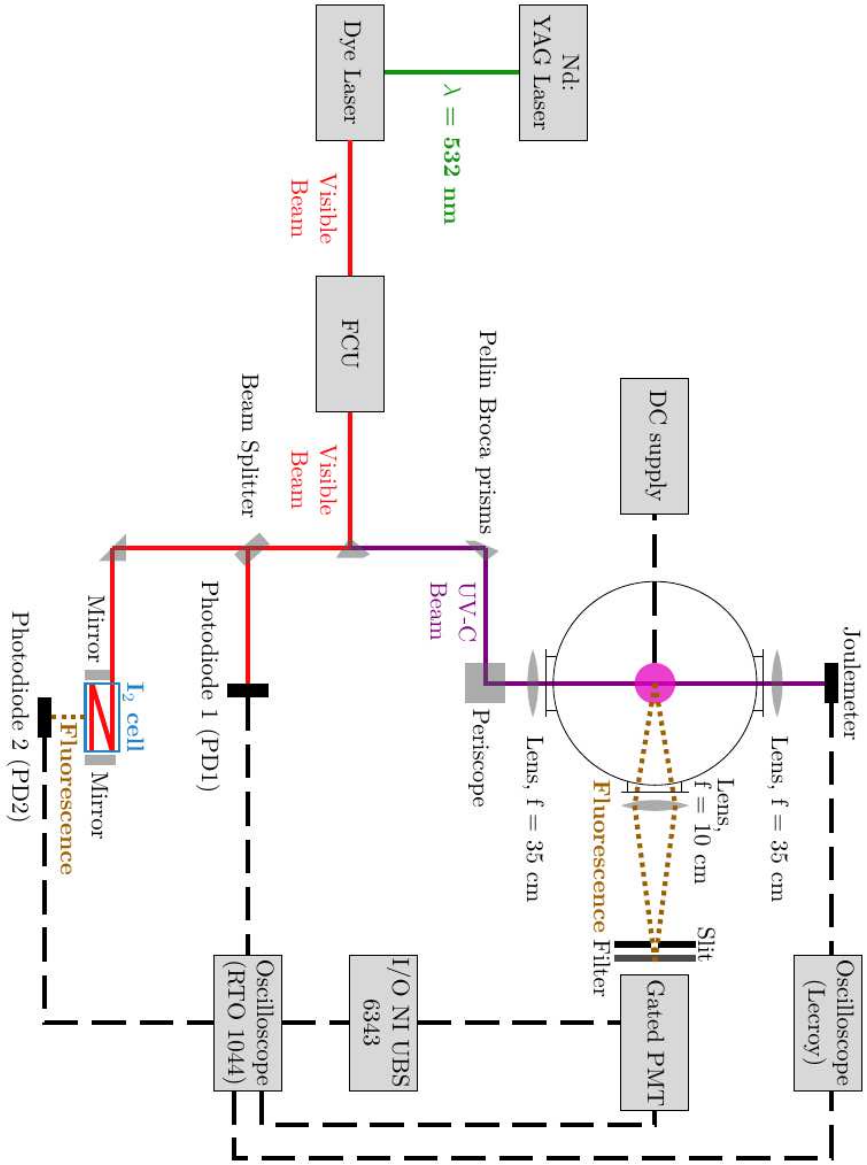

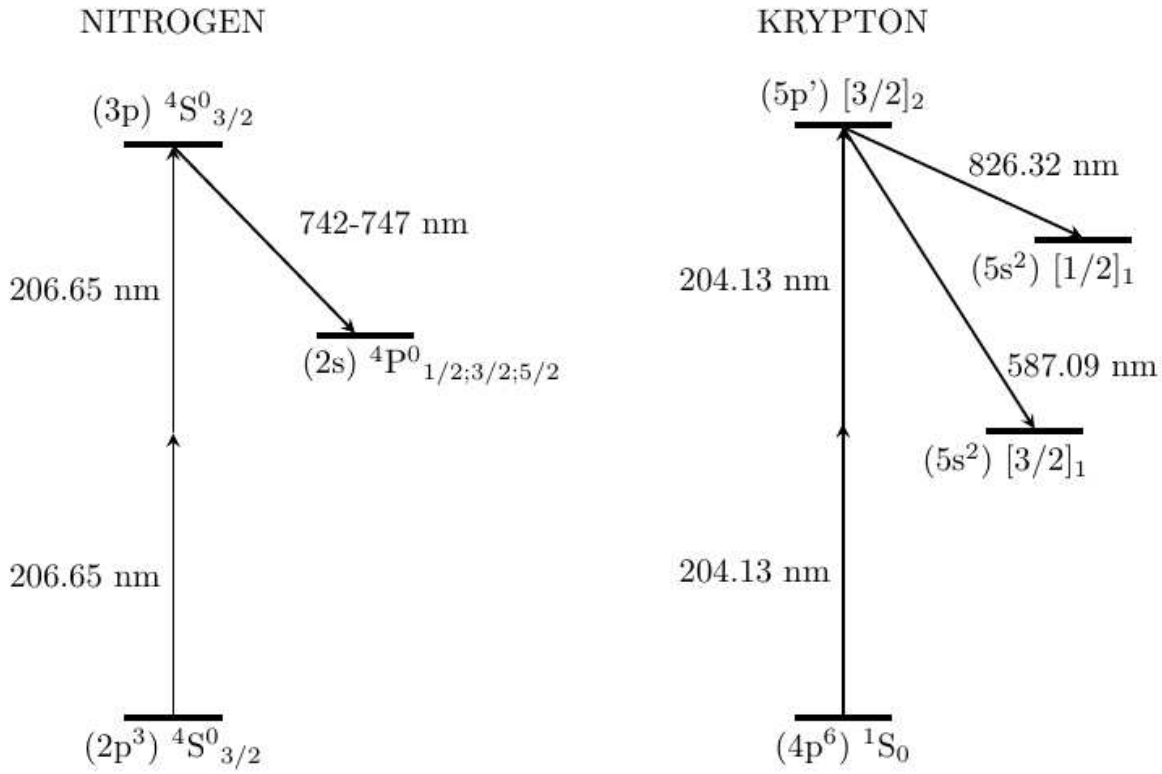

PLEASE CITE THIS ARTICLE AS DOI: 10.1063/5.0110318

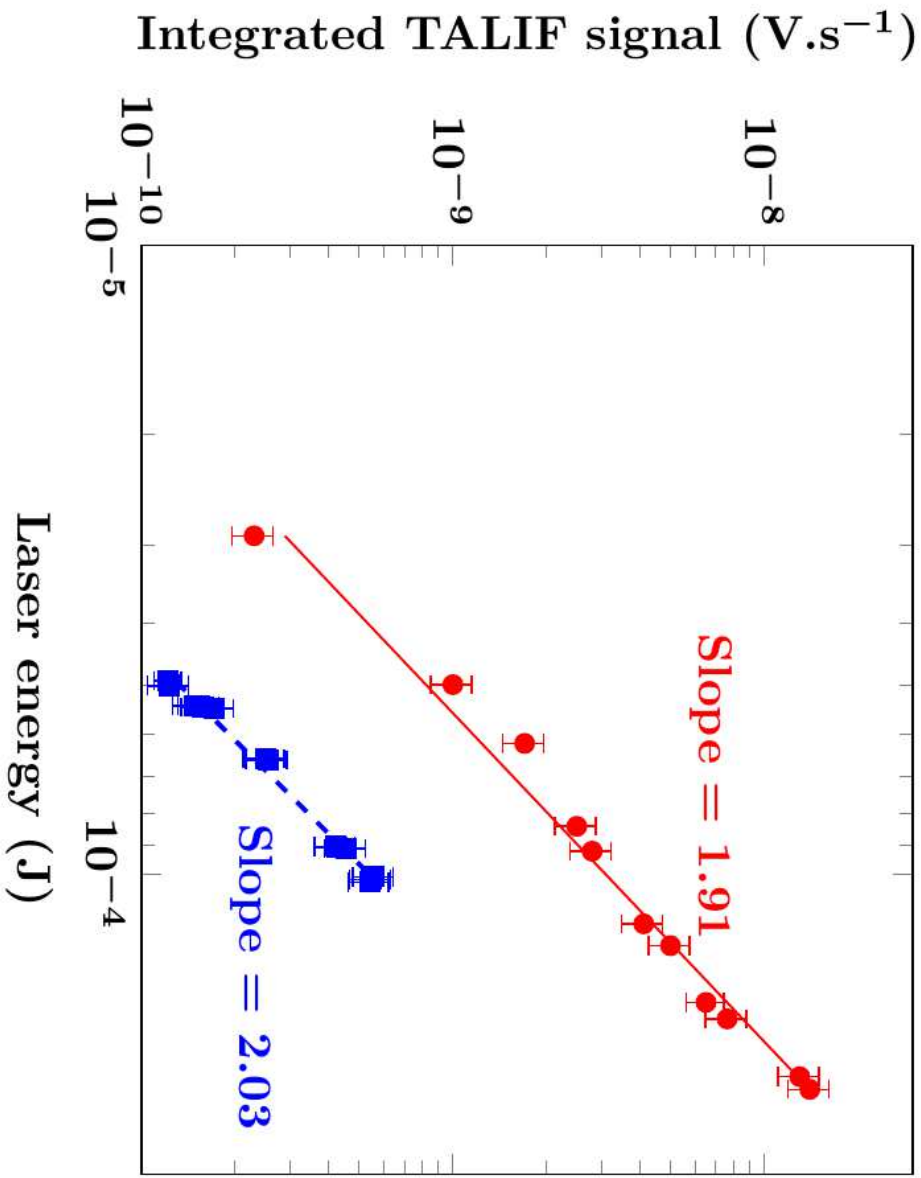

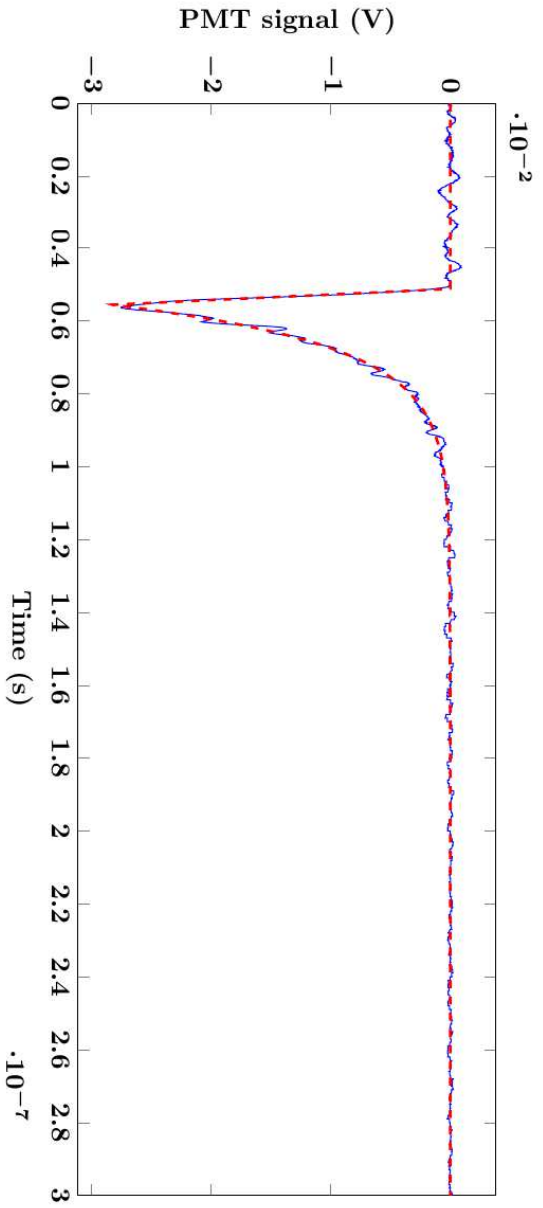

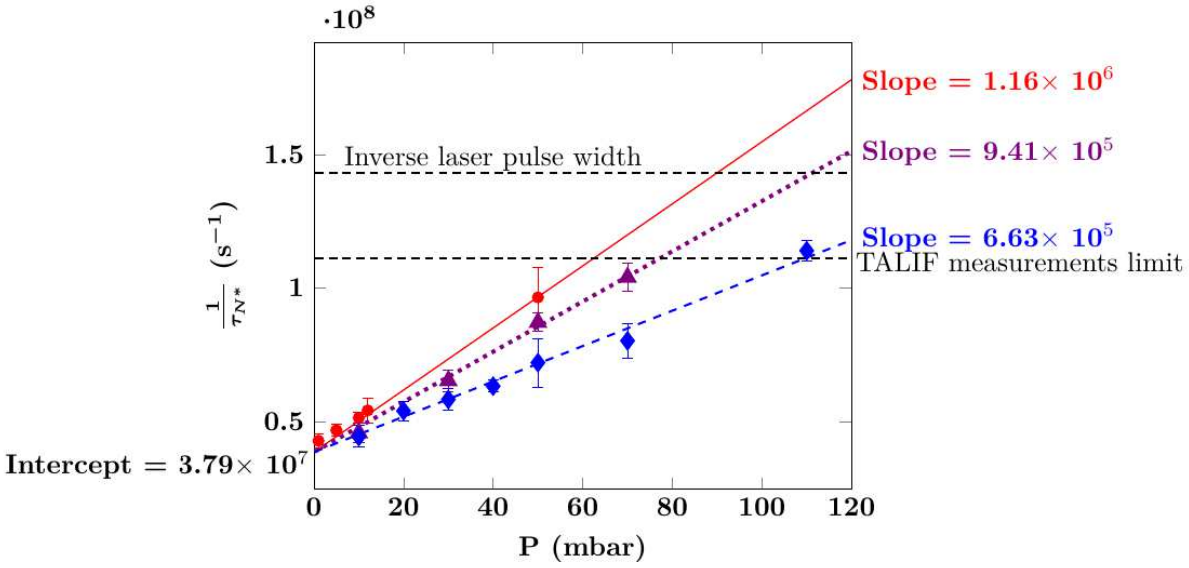

PLEASE CITE THIS ARTICLE AS DOI: 10.1063/5.0110318

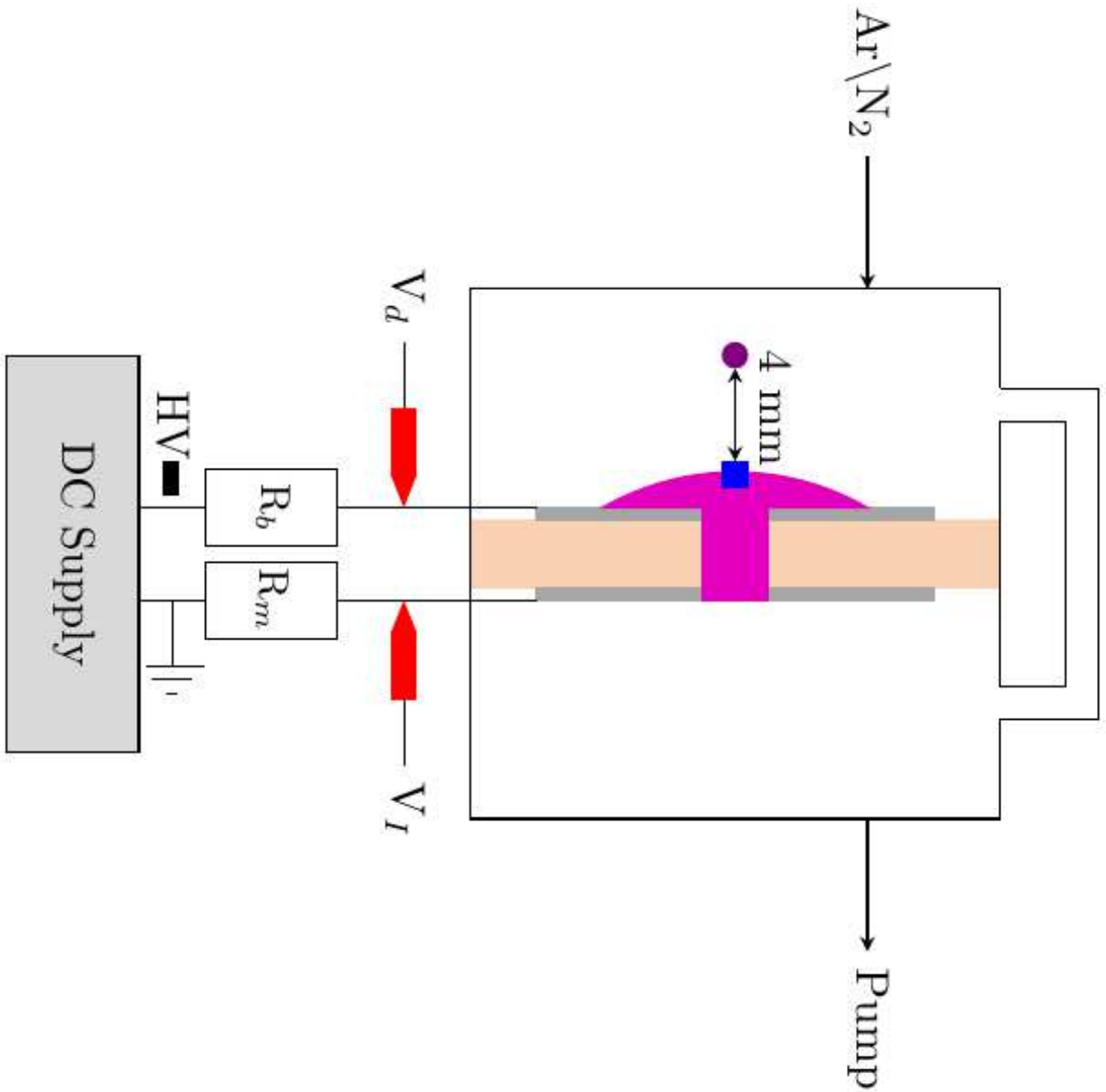

PLEASE CITE THIS ARTICLE AS DOI: 10.1063/5.0110318

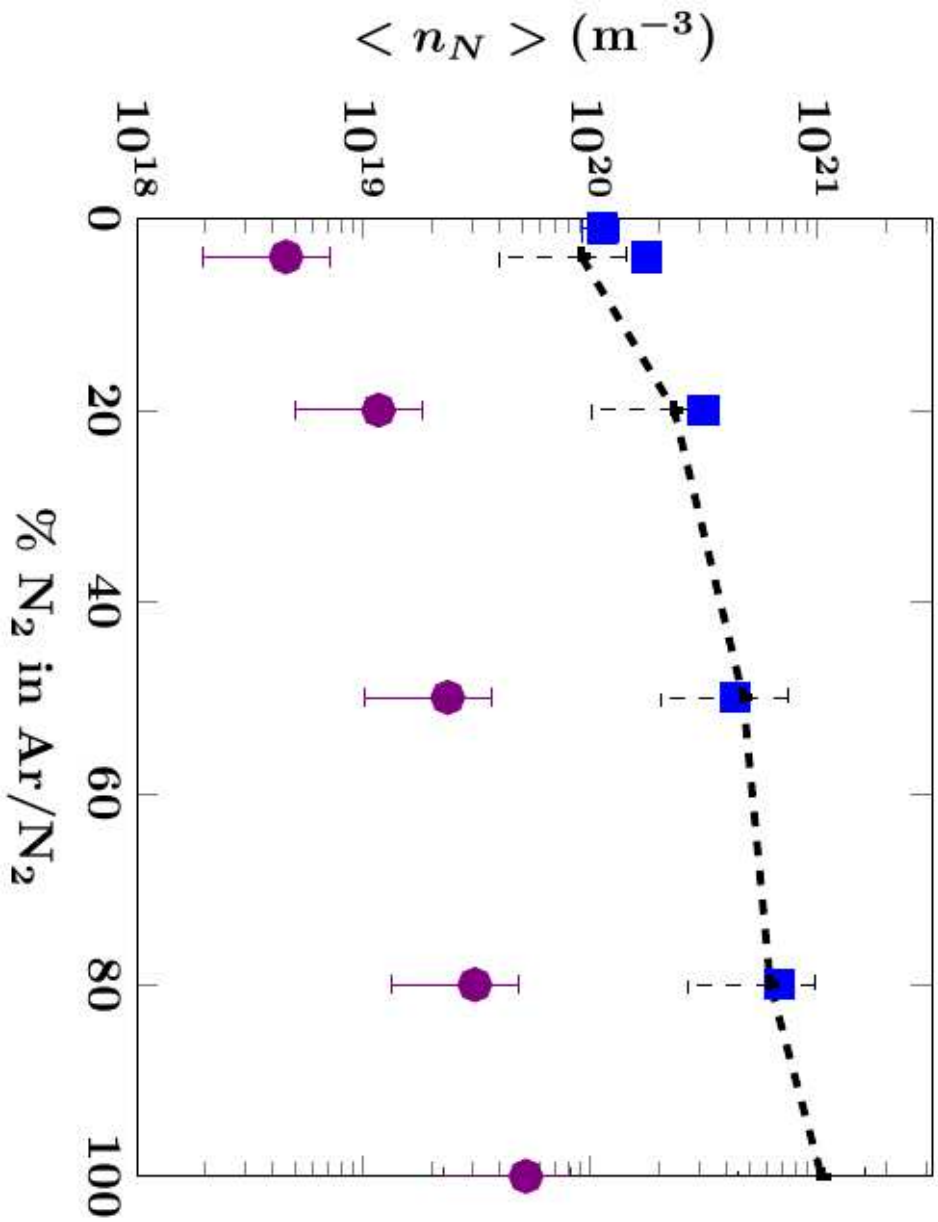

PLEASE CITE THIS ARTICLE AS DOI: 10.1063/5.0110318

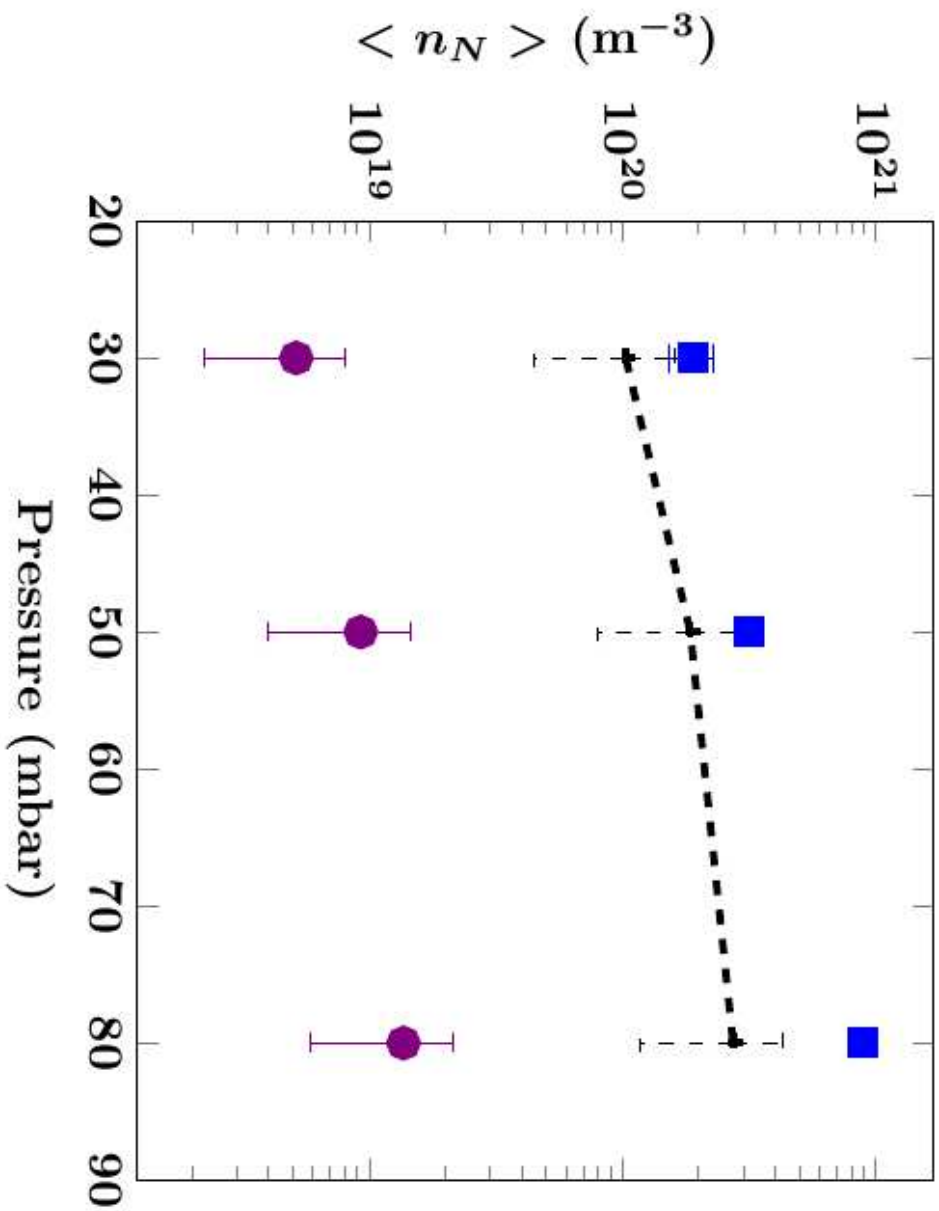

PLEASE CITE THIS ARTICLE AS DOI: 10.1063/5.0110318

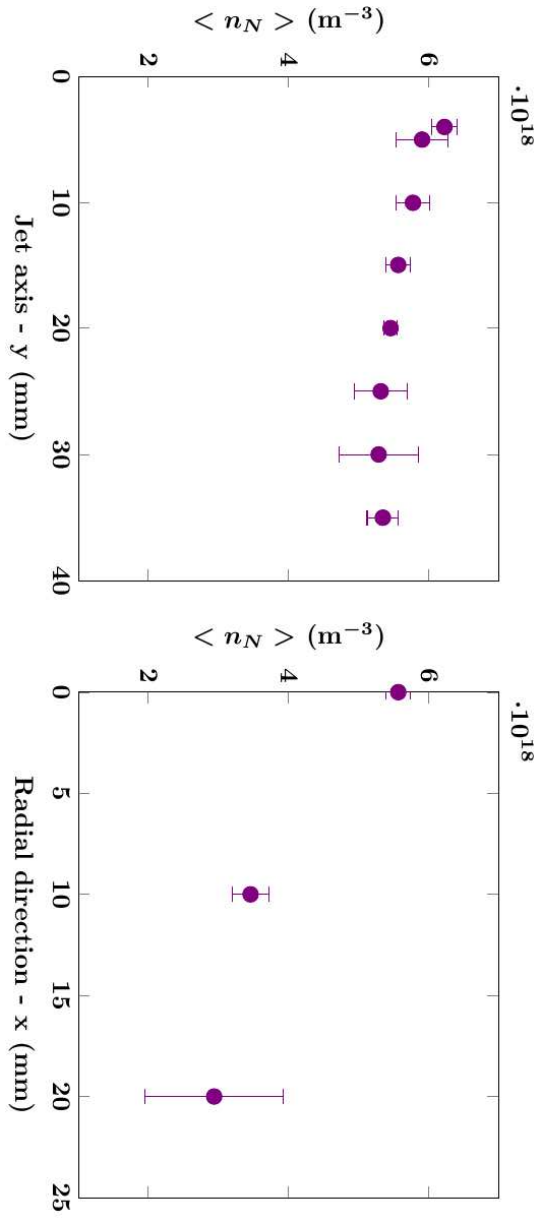

PLEASE CITE THIS ARTICLE AS DOI: 10.1063/5.0110318

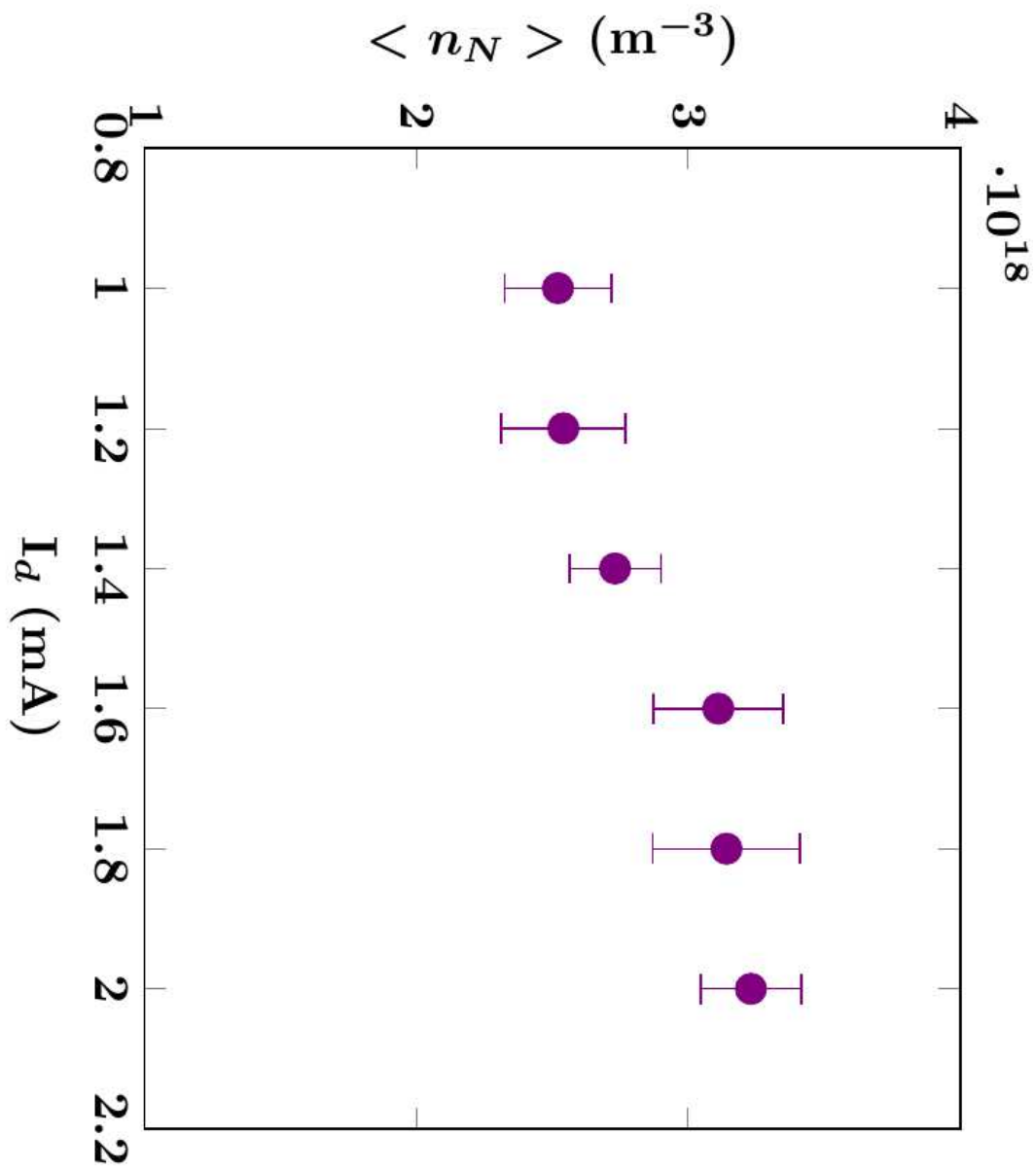

PLEASE CITE THIS ARTICLE AS DOI: 10.1063/5.0110318

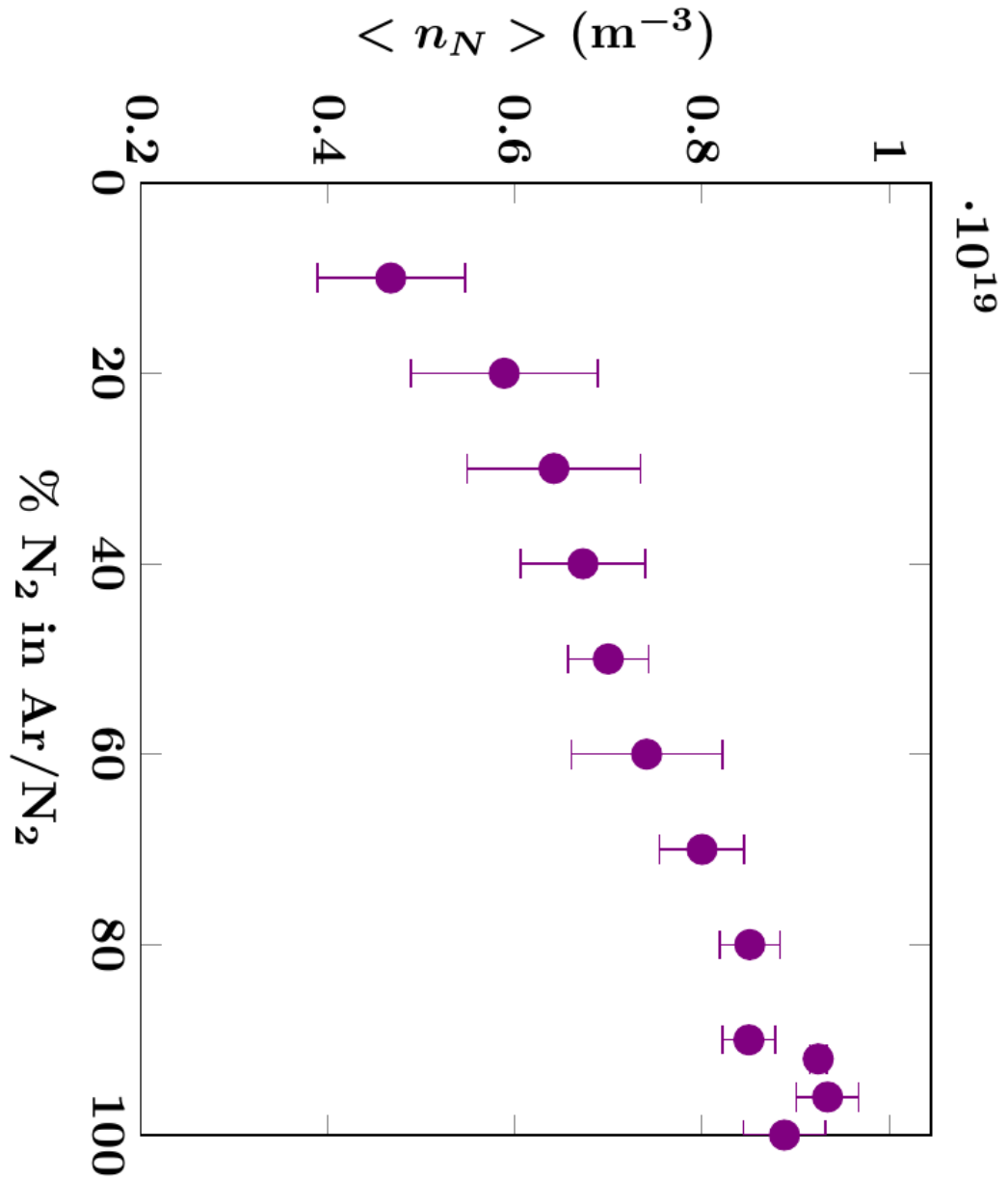

PLEASE CITE THIS ARTICLE AS DOI: 10.1063/5.0110318

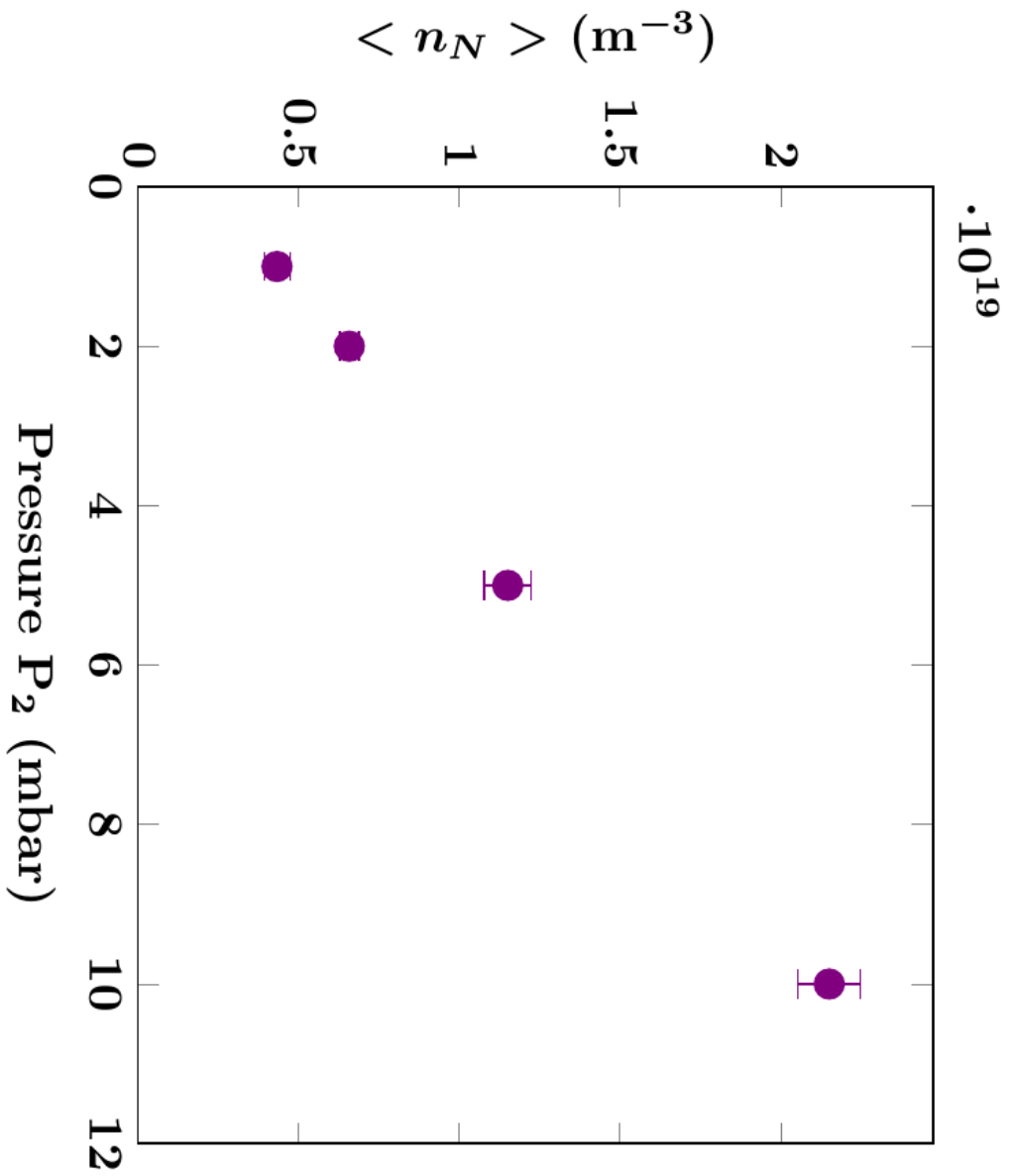

PLEASE CITE THIS ARTICLE AS DOI: 10.1063/5.0110318

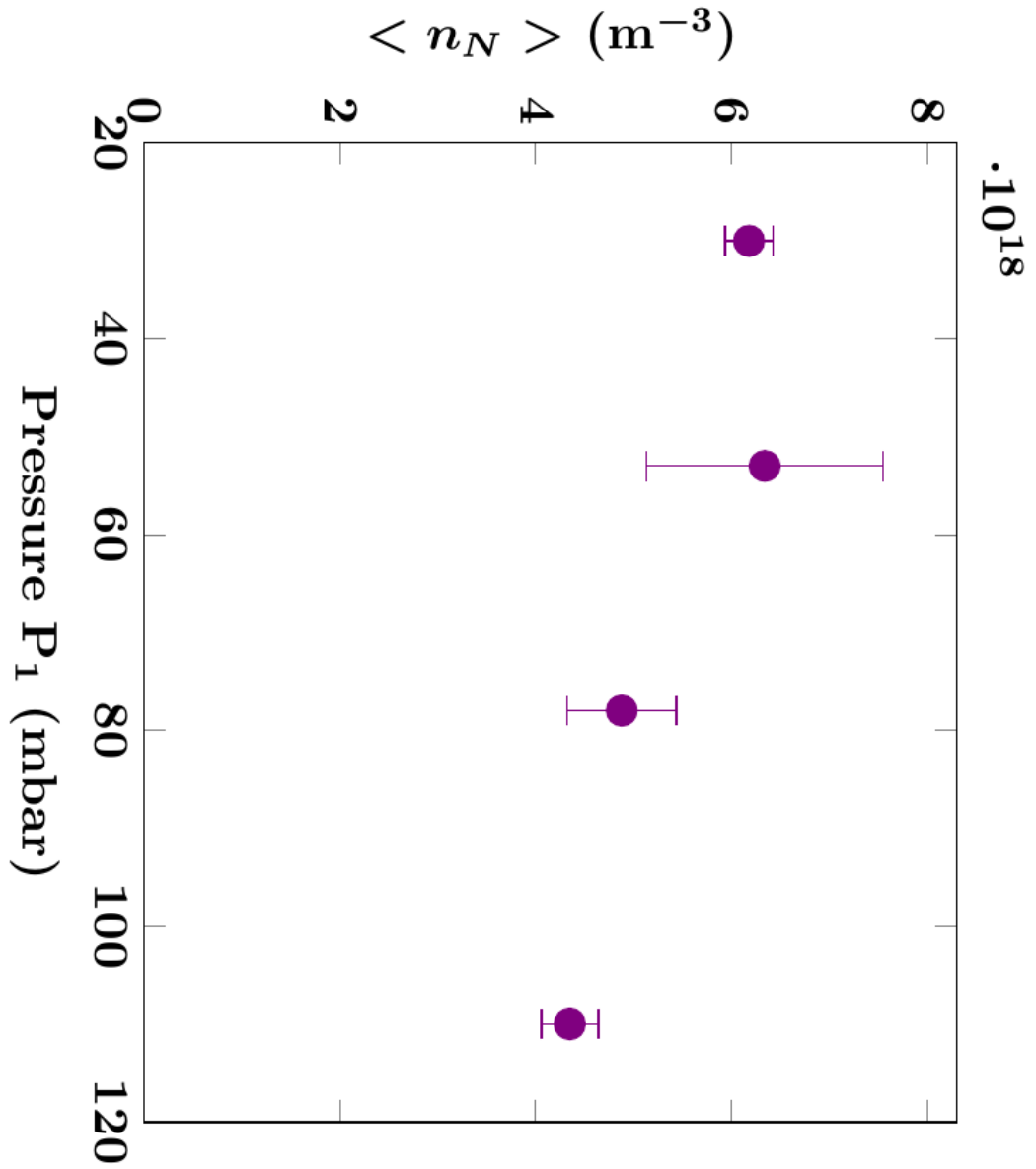

PLEASE CITE THIS ARTICLE AS DOI: 10.1063/5.0110318